

# Realistic models of general-relativistic differentially rotating stars

Marie Cassing<sup>1</sup>, Luciano Rezzolla<sup>1,2,3</sup>

<sup>1</sup>*Institut für Theoretische Physik, Max-von-Laue-Strasse 1, 60438 Frankfurt, Germany*

<sup>2</sup>*Frankfurt Institute for Advanced Studies, Ruth-Moufang-Strasse 1, 60438 Frankfurt, Germany*

<sup>3</sup>*School of Mathematics, Trinity College, Dublin 2, Ireland*

Accepted XXX. Received YYY; in original form ZZZ

## ABSTRACT

General-relativistic equilibria of differentially rotating stars are expected in a number of astrophysical scenarios, from core-collapse supernovae to the remnant of binary neutron-star mergers. The latter, in particular, have been the subject of extensive studies where they were modeled with a variety of laws of differential rotation with varying degree of realism. Starting from accurate and fully general-relativistic simulations of binary neutron-star mergers with various equations of state and mass ratios, we establish the time when the merger remnant has reached a quasi-stationary equilibrium and extract in this way realistic profiles of differential rotation. This allows us to explore how well traditional laws reproduce such differential-rotation properties and to derive new laws of differential rotation that better match the numerical data in the low-density Keplerian regions of the remnant. In this way, we have obtained a novel and somewhat surprising result: the dynamical stability line to quasi-radial oscillations computed from the turning-point criterion can have a slope that is not necessarily negative with respect to the central rest-mass density, as previously found with traditional differential-rotation laws. Indeed, for stellar models reproducing well the properties of the merger remnants, the slope is actually positive, thus reflecting remnants with angular momentum at large distances from the rotation axis, and hence with cores having higher central rest-mass densities and slower rotation rates.

**Key words:** stars: neutron – stars: rotation – stars: binaries – stars: kinematics and dynamics – equation of state – methods: numerical

## 1 INTRODUCTION

Multi-messenger astronomy and the detection of gravitational waves provide us with the possibility to study matter under extreme conditions such as supra-nuclear densities or ultra-strong gravity that are expected to be present in the remnants of a number of catastrophic astrophysical scenarios such as core-collapse supernovae (see, e.g., Ott et al. 2006; Burrows et al. 2007; Franceschetti & Del Zanna 2020), the accretion-induced collapse of white dwarfs (Dessart et al. 2006; Abdikamalov et al. 2010), the phase-transition-induced collapse of neutron stars (Lin et al. 2006; Abdikamalov et al. 2009), and, of course, the merger of two neutron stars (see, e.g., Shibata et al. 2003; Baiotti et al. 2008, for some initial works). A very important and distinctive feature of the rotational properties of these remnants is the presence of differential rotation, which is necessary to handle the large amounts of angular momentum that they inherit from the processes leading to their formation (see, e.g., Baiotti & Rezzolla 2017; Paschalidis 2017; Müller 2024, for some reviews). These differentially rotating compact stars are also known to be subject to non-axisymmetric deformations resulting from the development of dynamical instabilities (Rezzolla et al. 2000; Shibata et al. 2002; Saijo et al. 2003; Sá 2004; Baiotti et al. 2007; Manca et al. 2007; Krüger et al. 2010; Franci et al. 2013) and could lead to an interesting and peculiar gravitational-wave signal (see, e.g., Müller 2024, and references therein).

Since performing numerical simulations producing such differentially rotating remnants is extremely expensive, alternative approaches have long since been developed to study the properties of

these remnants in terms of self-gravitating configurations in equilibrium. The first studies in this direction have started in the 90's to study the equilibria of uniformly rotating relativistic stars (see, e.g., Komatsu et al. 1989a; Cook et al. 1992; Bonazzola et al. 1993; Stergioulas 1998, for some of the early and seminal works), and have revealed a number of properties of these objects. Among the most important of such properties we recall: the existence of a Keplerian stability line beyond which mass shedding occurs, the existence of a turning-point stability line which represents a sufficient but not necessary condition for the dynamical instability to gravitational collapse (Friedman et al. 1988; Takami et al. 2014), the proportionality between the maximum mass allowed by uniform rotation and the maximum mass of the corresponding nonrotating configuration (Cook et al. 1992; Lasota et al. 1996), which has then been shown to reflect a universal-relation for all equilibria along the turning-point stability line (Breu & Rezzolla 2016; Musolino et al. 2024).

All of these studies of uniformly rotating equilibria have represented the natural background, both in terms of astrophysical scenarios and of the numerical techniques employed, for the exploration of the more complex but also richer space of differentially rotating equilibria (Komatsu et al. 1989b; Goussard et al. 1998; Baumgarte et al. 2000; Lyford et al. 2003; Ansorg et al. 2009; Gondek-Rosińska et al. 2017; Studzińska et al. 2016; Bozzola et al. 2018; Weih et al. 2018; Skudlarek et al. 2019; Zhou et al. 2019; Espino & Paschalidis 2019; Bozzola et al. 2019; Zhou et al. 2019; Tsokaros et al. 2020; Staykov et al. 2023; Chi-Kit Cheong et al. 2024; Muhammed et al.

2024) and of their subsequent dynamics (Duez et al. 2006; Giacomazzo et al. 2011; Weih et al. 2018; Espino et al. 2019; Szweczyk et al. 2023).

Most the initial works exploring differentially rotating models exploited the simplest law of differential rotation, namely the “ $j$ -constant” (or KEH) law (Komatsu et al. 1989b), which, as by the name, imposes that the specific angular momentum  $j$  is constant across the star, so that the angular velocity essentially scales like  $1/r_e^2$ , where  $r_e$  is some measure of the distance from the rotation axis. However, as numerical simulations of BNS-mergers have started to explore in greater detail the properties of the merger remnant (see, e.g., Kastaun & Galeazzi 2015; Hanauske et al. 2017; Cioffi et al. 2017; De Pietri et al. 2018; East et al. 2019), it has appeared that the structure of the hypermassive neutron star (HMNS) produced after the merger is highly dynamical and non-trivial, but also that it can be interpreted effectively in terms of a simple mechanical toy model (Takami et al. 2015). Furthermore, the most salient rotational properties of the remnant are represented by: (i) a slowly and uniformly rotating core; (ii) a rapid increase in the angular velocity in the outer regions of the merger remnant; (iii) a radial fall-off reflecting a Keplerian profile.

As a consequence of this improved understanding of the rotational properties of BNS merger remnants, more realistic descriptions of the law of differential rotation have been suggested in the literature (see, e.g., Uryū et al. 2017; Passamonti & Andersson 2020; Xie et al. 2020; Camelió et al. 2021). Among the various suggestions for the differential-rotation law of BNS remnants, a parameterised family of angular velocity profiles has been suggested by Uryū et al. (2017), which in the 4-parameter version (U8 law) or in the 3-parameter (U9 law) prescription, provides a rather good description of the angular-velocity profiles of BNS remnants. This was shown first by Iosif & Stergioulas (2021) for simple polytropic equations of state (EOS) and later extended to tabulated EOSs in the comprehensive and detailed study of Iosif & Stergioulas (2022) for the 4-parameter version of the law.

While these laws have been extensively studied in the literature and applied to the analysis of differentially rotating neutron stars and quark stars, they do not always represent a good match to the simulations. To improve the level of realism in the construction of equilibrium models of differentially rotating neutrons stars, we have here reconsidered this problem with a bottom-up approach in which we first consider in detail the rotational information obtained from three, state-of-the-art BNS merger simulations performed with different and realistic EOSs and mass ratios. From these simulations we have then extracted the quasi-stationary rotational properties of the remnants, both in terms of azimuthally- and time-averaged profiles of the angular velocity and of the specific angular momentum. In this way, it was possible to study the existence of universal features in the angular-velocity profile and to point out a criterion that allows us to simply recognise the transition between the “core” of the remnant and the portion of the HMNS whose angular-velocity profile follows a Keplerian behaviour, i.e., the “disc”.

Using the differential-rotation profiles extracted from the simulations we have also improved the fidelity of the U9 law after a simple extension of the functional expression in terms of an additional exponent, leading to what we have referred to as the U9+ law. Because in the outer layers of the merger remnant the rest-mass density and the angular velocity are particularly low, both the U9 and the U9+ laws provide there rather inaccurate descriptions of the remnant properties. Hence, to counter that, we have devised a novel and more complex law of differential rotation, that we refer to as the CR law, which, allows us to reproduce with relative differences that

are always below 5% the angular-velocity profiles also well beyond the nominal stellar surface and in the disc.

As a final and particularly interesting aspect of our analysis, we have carried out the first systematic study of the properties of turning-point stability lines in realistic (and non-realistic) laws of differential rotation. In this way, we have obtained the surprising result that the slope of the stability line depends on the properties of the law of differential rotation and is not necessarily negative. In particular, those differential-rotations laws that provide an accurate representation of the simulated post-merger remnant lead to turning-point stability lines with positive slopes.

The structure of the paper is as follows. First we recall in Sec. 2 the theory of axisymmetric spacetimes and hydrostationary equilibria, as well as the numerical setup needed in the optimised Hydro-RNS code to compute such equilibria. Section 3 provides a quick review of the most traditional differential-rotation laws and shows our ability not only to reproduce published results with the U8 and U9 laws Iosif & Stergioulas (2021), but also to extend the space of solutions that can be obtained with them. Section 4 is dedicated to the analysis of the data of from the BNS-merger simulations and to illustrate how to determine the existence of a quasi-stationary equilibrium and to extract reliable profiles that are averaged in azimuthal angle and time; this section also provides a discussion on a simple criterion to determine the transition from the HMNS core to its disc. Section 5 proposes the new laws of differential rotation, providing evidence of their accuracy in reproducing the numerical data from the simulations and contrasting their performance in the various regions of the remnants; the section also discusses the properties of the turning-point stability lines and how their slope can be suitably modified across different differential-rotation laws. Finally, Sec. 6 provides a summary of our results and the prospects for future work. Hereafter, we adopt a set of units in which  $c = 1 = G$ , with  $c$  and  $G$  being the speed of light and the gravitational constant, respectively. Furthermore, we adopt Greek letters for indices running from 0 to 3 and Latin letters for indices running from 1 to 3.

## 2 THE THEORY OF ROTATING STARS: A BRIEF REVIEW

A neutron star in equilibrium can be described as a stationary axisymmetric self-gravitating perfect fluid whose equilibrium, using a Newtonian language, is governed by the balance between gravitational, rotational, and pressure-gradients forces. The corresponding stationary and axisymmetric spacetime can be described by the following metric in quasi-isotropic spherical coordinates

$$ds^2 = -e^{2\nu} dt^2 + e^{2\psi} (d\phi - \omega dt)^2 + e^{2\mu} (dr^2 + r^2 d\theta^2). \quad (1)$$

This spacetime is asymptotically flat and stationary, such that from the Killing vectors – defined as those along which Lie-derivative vanishes – can be found. The corresponding components are then given by  $t^\alpha$ ,  $\phi^\alpha$ , so that the coordinates  $t$  and  $\phi$  are cyclic [i.e., the metric (1) does not depend on them]. The quantity  $u^\alpha = dx^\alpha/d\tau$  is the four-velocity of the fluid with respect to the proper time  $\tau$  and, in the case of a circular motion in such a spacetime has components

$$u^\alpha = u^t (t^\alpha + \Omega \phi^\alpha), \quad (2)$$

where the angular velocity  $\Omega$  is defined as

$$\Omega := \frac{u^\phi}{u^t} = \frac{d\phi}{dt}. \quad (3)$$

We recall that, given the energy-momentum tensor of a perfect

fluid with energy density  $e$ , pressure  $p$  and four-velocity  $u^\mu$  is given by (see, e.g., [Rezzolla & Zanotti 2013](#))

$$T^{\mu\nu} = (e + p)u^\mu u^\nu + pg^{\mu\nu}, \quad (4)$$

the equations of hydrostationary equilibrium can be derived from the conservation of such tensor  $\nabla_\mu T^{\mu\nu} = 0$ . In particular, for a fluid with four-velocity components  $u^t$ , and  $u^\phi$ , we can write the equation of hydrostationary equilibrium for a rotating star as (or “rotation integral”)

$$\frac{\nabla_\alpha p}{(e + p)} = \nabla_\alpha \ln u^t - u^t u_\phi \nabla_\alpha \Omega. \quad (5)$$

It is now convenient to define the quantity

$$j := u^t u_\phi, \quad (6)$$

as the gravitationally redshifted specific angular momentum, which will play an important role in the investigation of rotation profiles of differentially rotating stars (We note that the quantity  $j$  is instead indicated as  $F$  in [Stergioulas \(1998\)](#), which is an important reference in the context equilibria of rotating stars). Using definition of the specific angular momentum (6), the Euler equation (5) can also be expressed in the form that will be useful later on

$$\frac{\nabla_\alpha p}{(e + p)} = \nabla_\alpha \ln u^t - j \nabla_\alpha \Omega. \quad (7)$$

Another useful quantity valid for barotropic fluids, i.e., fluids whose energy density depends only on the pressure, is the dimensionless enthalpy

$$H(p) := \int_0^p \frac{dp'}{e(p') + p'}, \quad (8)$$

which, after using the second law of thermodynamics, can be shown to satisfy the identity

$$\nabla H = \nabla \ln h - \frac{T}{h} \nabla s, \quad (9)$$

where  $\rho$  is the rest-mass density,  $T$  the temperature,  $s$  the specific entropy density, and  $h := (e + p)/\rho$  the specific enthalpy. As a result, the Euler equation (7) can be rewritten as

$$\nabla (H - \ln u^t) = -j \nabla \Omega, \quad (10)$$

where  $\Omega$  is either a constant in the case of uniformly rotating stars, or can be a function of position if the star is rotating differentially. Employing the relativistic version of the Poincaré-Wavre theorem ([Tassoul 1978](#)), the specific angular momentum is a function of the angular velocity only, i.e.,  $j = j(\Omega)$ , so that we can rewrite the Euler equation (10) in an integral form and obtain the first integral of hydrostationary equilibrium

$$H - \ln u^t + \int_{\Omega_0}^{\Omega} j(\Omega') d\Omega' = \text{const.} \quad (11)$$

In the case of uniform rotation and taking  $\Omega_0 = \Omega_{\text{pol}}$ , Eq. (10) reduces to  $H - \ln u^t = v|_{\text{pol}}$ , where  $v|_{\text{pol}}$  is the value of the metric function  $v$  at the pole. If  $\Omega$  is not uniform, Eq. (11) does not hold and the resulting rotation integral (5) will be a function of  $\Omega$ . Depending on the chosen rotation law  $j = j(\Omega)$ , the integral in (11) can either be computed analytically or, in more general conditions, it will have to be calculated numerically.

## 2.1 Numerical setup

The numerical calculations reported here have been performed making use of a modified version of the Hydro-RNS thorn, which is part of the Einstein-toolkit ([Haas & et al. 2020](#)). Hydro-RNS is based on the original RNS code ([Stergioulas & Friedman 1995; Stergioulas et al. 2004](#)) computes equilibrium solutions of rotating stars with analytic and tabulated EOSs that are either in uniform or differential rotation. In addition, by construction, it can compute sequences of stellar models having either constant central rest-mass densities  $\rho_c$ , or constant ratio between the polar and equatorial radii  $R_p/R_e$ . In practice, the code integrates the Einstein equations for stars described as perfect fluids employing the so-called Komatsu-Eriguchi-Hachisu (KEH) formulation in which the Einstein equations are rewritten as a set of elliptic equations and are solved using Green functions ([Komatsu et al. 1989a](#)). In particular, the rotating-star models are assumed to be described by the generic line-element

$$ds^2 = -e^{\gamma+\varrho} dt^2 + e^{\gamma-\varrho} r^2 \sin^2 \theta (d\phi - \omega dt)^2 + e^{2\alpha} (dr^2 + r^2 \sin^2 \theta), \quad (12)$$

where the metric functions  $\gamma$ ,  $\varrho$ ,  $\alpha$  and  $\omega$  depend only on the coordinates  $r$  and  $\theta$  ( $\omega$  accounts for the frame-dragging effect) and where the radial quasi-isotropic coordinate  $r$  is related to the proper circumferential radial coordinate  $R$  via the simple expression  $R := e^{\gamma-\varrho} r^2 \sin^2 \theta$ . We use small “ $r$ ” for quantities related to the quasi-isotropic radius as, for example,  $r_e$  and capital  $R$  for the corresponding proper value, that is the integral of the infinitesimal proper distance. The code uses the angular variable  $\mu := \cos(\theta)$  and compactifies the radial coordinate by  $s := r/(r_e + r)$ , such that  $s = 0.5$  at the equator  $r_e$ .

Quite generically, and independently of whether the rotation is uniform or differential, Hydro-RNS first computes the solution for a spherically symmetric configuration and uses it as an initial guess while slightly decreasing the axis ratio  $R_p/R_e$ . For each value of the latter, an iteration procedure to obtain an equilibrium stellar model is carried out, starting with guesses for the metric functions and ending if a desired accuracy in the quasi-isotropic equatorial radius  $r_e$  is reached. Given a first guess of the metric functions  $\rho$ ,  $\gamma$ ,  $\mu$ ,  $\omega$ , of the energy density  $\epsilon$  and of the angular velocity  $\Omega$  some of these quantities are rescaled to dimensionless units (denoted with a hat) to be used in the code, such as

$$\hat{\gamma} := \gamma/r_e^2, \quad \hat{\rho} := \rho/r_e^2, \quad \hat{\alpha} := \alpha/r_e^2, \quad (13)$$

$$\hat{\omega} := \omega r_e, \quad \hat{\Omega} := \Omega r_e. \quad (14)$$

In a second step, the radius at the equator  $r_e$  is calculated from the first integral of the hydrostationary equilibrium equated at the pole and at the centre. Next, the equatorial rotation frequency  $\Omega_e$  is obtained from equating the Euler equation at the pole and at the equator and finding the root with a Brent-algorithm. Since now that  $\Omega_e$  is found, the central rotation frequency  $\Omega_c$  is calculated accordingly from the rotation law. The whole distribution of angular velocity  $\Omega$  on the grid in  $s$  and  $\mu$  is obtained by finding the root of  $j(\Omega) = u^t u_\phi$  at each grid-point. Using the distribution  $\Omega(s, \mu)$ , it is possible to calculate the velocity of the fluid  $v(s, \mu)$  and the specific enthalpy at each grid-point  $h(s, \mu)$  through the equation of hydrostationary equilibrium (11). At this stage, using the specific enthalpy  $h(s, \mu)$  it is possible to calculate at each grid-point thermodynamic quantities such as the pressure and energy density. In the last step of the iteration over  $r_e$ , the metric functions and the metric potentials  $S_\gamma$ ,  $S_\rho$ ,  $S_\omega$  and  $S_\alpha$  are calculated. After that the procedure is repeated until convergence is reached.

Once a solution for a rotating stellar model with the desired accuracy is found, the corresponding integral quantities, such as the gravitational mass  $M$  or the angular momentum  $J := \int j dM_0$  (with baryonic mass  $M_0$ ), can be used to construct sequences. Particularly useful are sequences of stellar models having the same angular momentum  $J$ , as these sequences are normally characterised by a maximum value of the gravitational mass, that is a mass satisfying the condition

$$\left. \frac{\partial M}{\partial \rho_c} \right|_J = 0. \quad (15)$$

A well-known criterion, the “turning-point” criterion (Friedman et al. 1988) then states that the condition (15) is a sufficient condition for the quasi-radial dynamical instability leading to a gravitational collapse to black holes. A less well-known result is that the “turning-point stability line”, i.e., the line marked by all stellar models satisfying Eq. (15), is distinct (for  $J > 0$ ) from the “neutral-stability line”, which is instead marked by all stellar models whose fundamental  $f$ -mode frequency vanishes (Takami et al. 2011). By construction, and independently of the type of rotation law, such a line represents a necessary condition for the appearance of a dynamical instability leading to a gravitational collapse, hence, truly distinguishing stellar models that are unstable from those that are instead stable. Unfortunately, the neutral-stability line can be determined either via complex perturbative studies (Dimmelmeier et al. 2006; Zink et al. 2010; Takami et al. 2011) or through direct numerical-relativity calculations (Font et al. 2002; Takami et al. 2011; Weih et al. 2018; Szweczyk et al. 2023). Because of its simplicity, and bearing in mind that the differences between the two lines in terms of masses and central rest-mass densities are of a few percent at most, we will hereafter make use only of the turning-point stability line.

### 3 TRADITIONAL DIFFERENTIAL-ROTATION LAWS

Several laws of differential rotation that are meant to mimic those encountered in the HMNS produced in a BNS merger have been proposed over the years and a particularly rich family has been proposed in Uryū et al. (2017), and feature the presence of a peak in the rotation profiles together with a (Keplerian) fall-off. Within this family of rotation laws, two are particularly interesting and have been employed in previous works, namely, [see Eq. (8) of Uryū et al. (2017)]

$$\Omega(j, A, B, p, q) = \Omega_c \frac{1 + (j/(B^2 \Omega_c))^p}{1 + (j/(A^2 \Omega_c))^{(q+p)}} \quad (16)$$

and [see Eq. (9) of Uryū et al. (2017)]

$$\Omega(j, A, B, p) = \Omega_c \left( 1 + \left( \frac{j}{B^2 \Omega_c} \right)^p \right) \left( 1 - \left( \frac{j}{A^2 \Omega_c} \right) \right), \quad (17)$$

and hereafter we will refer them as the “Uryu-8” (U8) and “Uryu-9” (U9) laws, respectively (Uryū et al. 2017). Note that the first law (16) has four parameters,  $p, q, A, B$ , while the second one (17) has only three,  $p, A, B$ . Furthermore, because these laws are expressed as functions  $\Omega = \Omega(j)$  and not in the inverse form  $j = j(\Omega)$  needed to fulfil the integrability condition, it is necessary to perform a variable transformation

$$\int j d\Omega = \int j \frac{d\Omega}{dj} dj, \quad (18)$$

to compute the integral of the Euler equation (11).

#### 3.1 The Uryu-8 rotation law

In this subsection we focus on the properties of the U8 law (16) first concentrating on solutions obtained when varying two relevant parameters ( $\lambda_1$  and  $\lambda_2$ ; see Sec. 3.1.1 for a definition) and then when considering variations of all parameters (Sec. 3.1.2).

##### 3.1.1 Varying $\lambda_1$ and $\lambda_2$

We start by recalling that the shape of the rotation profile  $\Omega = \Omega(R)$  is mainly changed by the parameter  $A$ , which essentially sets the outer radius of the star, and by the parameter  $B$ , which essentially sets the maximum of the angular velocity. At the same time, rather than working directly with the parameters  $A$  and  $B$ , it is more convenient to work through suitable combinations of them. More specifically, following the parameterisation first suggested by Iosif & Stergioulas (2021), we introduce the new parameters  $\lambda_1$  and  $\lambda_2$  that are functions of  $A$  and  $B$  and essentially parameterisations of the maximum angular velocity  $\Omega_{\max}$  and of angular velocity at the equator  $\Omega_e := \Omega(R = R_e)$  in terms of the central angular velocity  $\Omega_c := \Omega(R = 0)$

$$\lambda_1 := \frac{\Omega_{\max}}{\Omega_c} = \frac{1 + (j_{\max}/(B^2 \Omega_c))^p}{1 + (j_{\max}/(A^2 \Omega_c))^{(q+p)}}, \quad (19)$$

$$\lambda_2 := \frac{\Omega_e}{\Omega_c} = \frac{1 + (j_e/(B^2 \Omega_c))^p}{1 + (j_e/(A^2 \Omega_c))^{(q+p)}}. \quad (20)$$

A maximal rotation is achieved at an angular momentum  $j_{\max}$ . In practice, because Hydro-RNS employs dimensionless quantities, we use the equatorial radius  $r_e$  to compute the “hatted” quantities

$$\hat{j}_{\max} := j_{\max}/r_e, \quad \hat{j}_e := j_e/r_e, \quad (21)$$

$$\hat{\Omega}_e := \Omega_e r_e, \quad \hat{\Omega}_{\max} := \Omega_{\max} r_e. \quad (22)$$

so that we can compute the angular velocity at the equator by equating the Euler equation at the pole with its value at the equator

$$0 = \ln \left( \frac{u_{\text{pol}}^t}{u_{\text{eq}}^t} \right) + \int_0^{\hat{r}_e} j \frac{d\Omega}{dj} dj. \quad (23)$$

Using in Eq. (23) the metric (12) and the four-velocity component  $u^t$ ,

$$u^t = \frac{e^{-(\gamma+\rho)/2}}{\sqrt{1-\nu^2}}, \quad \nu = (\Omega - \omega) r \sin \theta e^{-\rho}, \quad (24)$$

we obtain an expression in dimensionless units, which we solve by a Brent-method

$$0 = r_e^2 (\hat{\gamma}_e + \hat{\rho}_e - \hat{\gamma}_p - \hat{\rho}_p) + \ln \left[ 1 - (\hat{\Omega}_e - \hat{\omega}_e)^2 e^{-2r_e^2 \hat{\rho}_e} \right] + 2 \int_0^{\hat{r}_e} j \frac{d\Omega}{dj} dj. \quad (25)$$

where

$$\hat{j}_e = \frac{(\hat{\Omega}_e - \hat{\omega}_e)^2 e^{-2r_e^2 \hat{\rho}_e}}{1 - (\hat{\Omega}_e - \hat{\omega}_e)^2 e^{-2r_e^2 \hat{\rho}_e}}, \quad (26)$$

represents the dimensionless specific angular momentum at the equator.

Since  $r_e$  is a function of the axis ratio and exhibits a maximum  $r_{e,\max}$  at some value of the axis ratio  $(R_e/R_p)_{\max}$ , experience has shown that in order to solve Eq. (25), the guesses of the iterated



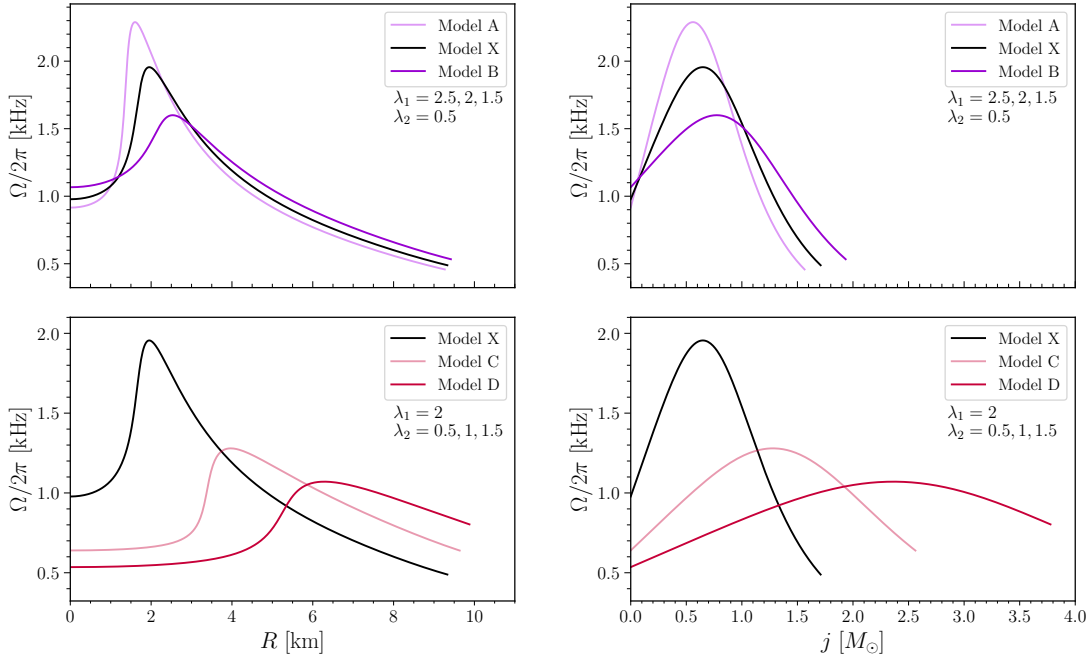


**Figure 1.** Angular velocity as a function of the proper circumferential radial coordinate  $R$  (left panel) and angular velocity as a function of the specific angular momentum  $j$  (right panel) for a stellar model obeying the DD2 EOS, having a central rest-mass density  $\rho_c = 8.024 \times 10^{14} \text{ g cm}^{-3}$ , and an axis ratio  $R_p/R_e = 0.8$ . The underlying differential rotation law is U8 with  $p = 1$ ,  $q = 3$  and varying parameters  $\lambda_1$ ,  $\lambda_2$ .

quantity  $r_e$  for the U8 law should be close to the values given by the function

$$r_e = r_{e,\max} - k_1 \left[ (R_e/R_p)_{\max} \right]^{k_2}, \quad (27)$$

which depends on the chosen rotation parameters or on the central rest-mass density; we found that  $k_2 = 2.62$  approximates well guesses for different central rest-mass densities. The parameter  $k_1$  in Eq. (27) can be calculated as

$$k_1 = ((r_{e,\max} - r_{e,\text{curr}}) / ((R_e/R_p)_{\max} - (R_e/R_p)_{\text{curr}}))^{k_2}, \quad (28)$$

where  $(R_e/R_p)_{\text{curr}}$  and  $r_{e,\text{curr}}$  are respectively the axis ratio at the current iteration and the corresponding equatorial (coordinate) radius and if the iteration scheme has reached some axis ratio beyond the maximum  $(R_e/R_p)_{\max}$ . The value of the maximum dimensionless specific angular momentum  $\hat{j}_{\max}$  is obtained numerically from the profile  $\Omega(j)$  where the parameters  $\hat{A}$  and  $\hat{B}$  are obtained from Eqs. (A5) and (A6) in [Iosif & Stergioulas \(2021\)](#). Once  $\Omega_e$  and  $\lambda_2$  are known, we use Eq. (20) to obtain the angular velocity at the center, i.e.,  $\Omega_c = \Omega_e / \lambda_2$ .

As discussed by [Iosif & Stergioulas \(2021\)](#), the rotational integral in (23) has an analytical solution for the specific set of parameters  $p = 1$  and  $q = 3$ , in which case it reads

$$\begin{aligned} \int_0^j j' \frac{d\Omega}{dj'} dj' &= j\Omega - \frac{A^4 \Omega_c^2}{2B^2} \arctan \left( \frac{j^2}{A^4 \Omega_c^2} \right) \\ &\quad - \frac{\sqrt{2} A^2 \Omega_c^2}{4} \left[ \arctan \left( 1 - \frac{j\sqrt{2}}{A^2 \Omega_c} \right) \right. \\ &\quad \left. - \arctan \left( 1 + \frac{j\sqrt{2}}{A^2 \Omega_c} \right) + \tanh^{-1} \left( \frac{A^2 \Omega_c j \sqrt{2}}{j^2 + A^4 \Omega_c^2} \right) \right], \end{aligned} \quad (29)$$

where we have used the identity:  $\tanh^{-1}(x) = 0.5 \ln((1+x)/(1-x))$ .

How the parameters  $\lambda_1$  and  $\lambda_2$  change the shape of the rotation

profiles can be appreciated from Fig. 1, where we report models computed for the DD2 EOS ([Hempel & Schaffner-Bielich 2010b](#)) at a fixed central rest-mass density of  $\rho_c = 8.024 \times 10^{14} \text{ g cm}^{-3}$ , an axis ratio  $R_e/R_p = 0.8$ , and with  $p = 1$ ,  $q = 3$ . Note how the parameter  $\lambda_1$  mostly affects the height of the maximum of the angular velocity (top row), while its position is only minimally affected; in all cases, the equatorial angular velocity is smaller than the central one. Small are also the changes in the profiles of  $\Omega(j)$ , which essentially reflect those in  $\Omega(R)$ . On the other hand, the parameter  $\lambda_2$  controls both the value of the equatorial angular velocity  $\Omega_e$  and the position of the angular-velocity maximum (bottom row). Note how  $\lambda_2$  also controls the slope of  $\Omega(j)$ , leading to much smaller gradients and increasing the maximum value of the specific angular momentum at the equator. The equilibrium properties as the total mass or equatorial radius of all Models can be found in Table A1 in Appendix A.

The full space of solutions of differentially rotating stars obtained with the DD2 EOS and the parameters choice  $p = 1$ ,  $q = 3$ ,  $\lambda_1 = 1.5$ , and  $\lambda_2 = 0.5$  is shown in Fig. 2 in the  $(M, \rho_c)$  plane and matches the equivalent Fig. 3 of [Iosif & Stergioulas \(2022\)](#), where the central energy density is used instead. Shown with grey solid lines of different transparency we report  $J = \text{const.}$  sequences, with  $J \in [0.25, 9.5]$  ([light-grey, dark-grey]). As discussed in the Introduction, the maxima of these sequences of constant  $J$  mark turning-point stability line (light-blue solid line). The stability line starts at the maximal mass  $M_{\text{TOV}}$  (black filled circle) of the static configurations, i.e., with  $\Omega = 0$  (blue solid line), crosses the Keplerian limit of uniformly rotating configurations, i.e., with  $\Omega = \Omega_{\text{K,ur}}$  (blue dashed line) at a mass  $M_{\text{tp;K,ur}}$  (blue filled square) and terminates with a model having a mass of  $M = 3.474 M_\odot$  (green filled circle); this value exceeds the maximum mass along the turning-point stability line reported by [Iosif & Stergioulas \(2022\)](#) (green cross) and has been achieved thanks to the additional iteration control in the extended version of our code. Note that for this EOS, the maximum mass of the Keplerian configurations with uniform rotation  $M_{\text{max;K,ur}}$  (blue

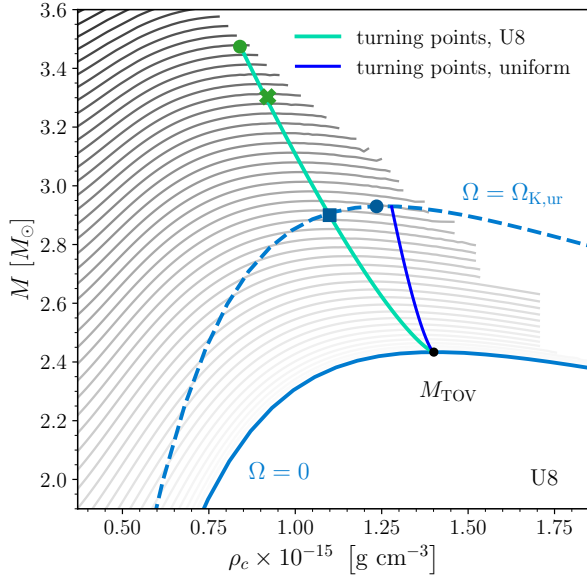


**Figure 2.** Total mass  $M$  as function of the central rest-mass density  $\rho_c$  for stellar models obeying the DD2 EOS and following the U8 differential-rotation law. Shown with grey shadings are sequences of constant total angular momentum  $J \in [0.25, 9.5]$  and the corresponding turning-point stability line (light-blue), which starts at  $M_{\text{TOV}}$  (black circle). The green cross marks the maximum mass reached previously by Iosif & Stergioulas (2022) on the stability line for this differential-rotation law and the green circle the corresponding maximum mass reached in this work. Also marked are the nonrotating sequence ( $\Omega = 0$ ) and the Keplerian stability line  $\Omega = \Omega_{\text{K,ur}}$  of uniformly rotating models with the same EOS; on such a line we mark the maximum mass (filled blue circle) and the maximum mass along the turning-point stability line (filled blue square). Finally, shown as a reference with a blue solid line is the turning-point stability line for the uniformly rotating models.

filled circle) is different and actually larger than  $M_{\text{tp;K,ur}}$  so that the corresponding stellar model is very likely to be dynamically unstable (see also Takami et al. 2011). As we will comment later on, the fact that  $M_{\text{tp;K,ur}} \leq M_{\text{max;K,ur}}$  appears to be a robust result quite independently of the EOS and law of differential rotation (see Figs. 5 and 10). Note that despite the improvements to the code and the solution strategy, our turning-point stability line does not cross the Keplerian sequence for this EOS and the U8 law. This will be possible only for the  $j$ -constant law and  $\hat{A} \gtrsim 3.33$  (see Fig. 13 but also Weih et al. (2018)).

### 3.1.2 Varying $A, B, p$ and $q$

We next consider the impact on the differential-rotation law when varying the parameters  $A$  and  $B$  rather than  $\lambda_1$  and  $\lambda_2$  (the values of  $p$  and  $q$  will be set to be constant as in Sec. 3.1.1). The advantage of this choice is that via the parameter  $B$  it is possible to scale the height of the values of central and maximum angular velocity, while via the parameter  $A$  it is possible to set the position of the maximum in radial direction. Since we are using  $A, B$  instead of  $\lambda_1, \lambda_2$ , we need to compute the latter from our choices for  $\hat{A} = A/r_e$  and  $\hat{B} = B/r_e$ . In particular, the parameter  $\lambda_2$ , i.e., the ratio  $\Omega_e/\Omega_c$  can be calculated as a root of the following nonlinear equation

$$0 = \frac{1 + (j_e \lambda_2 / (B^2 \Omega_e))^p}{1 + (j_e \lambda_2 / (A^2 \Omega_e))^{q+p}} - \lambda_2, \quad (30)$$

while  $\lambda_1$  can be computed through Eq. (19) once  $\Omega_c$  is found.

To illustrate the impact of the variation of the parameters  $\hat{A}, \hat{B}, p$  and  $q$  we consider the DD2 EOS and set as reference “Model Y”, that is, a star with  $\rho_c = 8.024 \times 10^{14} \text{ g cm}^{-3}$ ,  $\hat{A} = 1.8$ ,  $\hat{B} = 1.4$ ,  $p = 1$ , and  $q = 3$ . Such a model, which has a mass  $M_Y = 2.29 M_\odot$  a circumferential equatorial radius of  $R_{e,Y} = 9.84 \text{ km}$  and an axis ratio  $R_p/R_e = 0.8$  is reported with solid red lines in all panels of Fig. 3.

More specifically, the top-left panel of Fig. 3 highlights the impact of varying  $\hat{B}$  while leaving all the other parameters fixed (i.e.,  $\hat{A} = 1.8$ ,  $p = 1$ ,  $q = 3$ ) shows that it impacts the position and value of  $\Omega_{\text{max}}$ , as well as the value of  $\Omega_c$ , while leaving mostly unaffected the radial slope between  $\Omega_{\text{max}}$  and  $\Omega_e$  (see inset). Similarly, the top-right panel of Fig. 3 shows the changes introduced when varying  $\hat{A}$  and  $\hat{B}$ , but maintaining a constant ratio  $\hat{B}/\hat{A}$  to exclude large changes in  $\lambda_1$  and keeping the other parameters as in the top-left panel (i.e.,  $p = 1$ ,  $q = 3$ ). Clearly, as the values of  $\hat{A}$  and  $\hat{B}$  increase (i.e., going from model G to model H) the rotation profile changes considerably, with the maximal angular velocity, moving to larger radii and larger angular momenta. Indeed, model H is the one with the largest angular momenta and with the outermost location of the angular-velocity maximum.

Because our version of Hydro-RNS can handle values of the exponents  $p$  and  $q$  in a rather wide range, a large space of parameters can be explored in this way and a summary of this exploration is shown in the bottom panels of Fig. 3. In particular, the bottom left reports different models obtained when varying  $p$  while keeping the other parameters fixed, i.e.,  $\hat{A} = 1.8$ ,  $\hat{B} = 2$ , and  $q = 3$ ; in a similar fashion, the bottom right panel models are obtained varying  $q$  while keeping  $\hat{A} = 1.8$ ,  $\hat{B} = 2$ , and  $p = 1$ . Considering model Y, (red solid line) as the reference as it appears in all panels, it is possible to appreciate that an increase in  $p$  leads to more extended stars, spanning larger angular momenta and having an angular-velocity maximum farther away from the center. By contrast, an increase in  $q$  leads to more compact stars, spanning smaller angular momenta and having an angular-velocity maximum that is both larger and closer to the center. Also in this case, additional details on the various stellar models can be found in Table A1 in Appendix A.

### 3.2 The Uryu-9 rotation law

We next concentrate on the rotation profiles and hydrostatic equilibria that can be computed with the U9 rotation law (17). This law has a number of advantages. First, the derivatives and rotation integral can be calculated analytically for all possible parameters and not only for a specific parameter choice as for the U8 law with  $p = 1$ ,  $q = 3$ . Second, the law is fully described by a set of only three free parameters  $p, A, B$  instead of four as in U8. Finally, its functional form is such that it can produce solutions in the angular-velocity profile exhibiting an additional minimum close to the center of the star. We recall that the U9 rotation law reads as (Uryū et al. 2017)

$$\Omega(j) = \Omega_c \left( 1 + \left( \frac{j}{B^2 \Omega_c} \right)^p \right) \left( 1 - \left( \frac{j}{A^2 \Omega_c} \right) \right), \quad (31)$$

and it is possible to calculate analytically the first and second derivative of the angular velocity as

$$\frac{d\Omega}{dj} = \frac{p}{j} (A^2 \Omega_c - j) \left( \frac{j}{B^2 \Omega_c} \right)^p - \frac{1}{A^2} \left[ 1 + \left( \frac{j}{B^2 \Omega_c} \right)^p \right], \quad (32)$$

$$\frac{d^2\Omega}{dj^2} = -\frac{p}{A^2 j^2} (-A^2 \Omega_c p + A^2 \Omega_c + p j + j) \left( \frac{j}{B^2 \Omega_c} \right)^p, \quad (33)$$

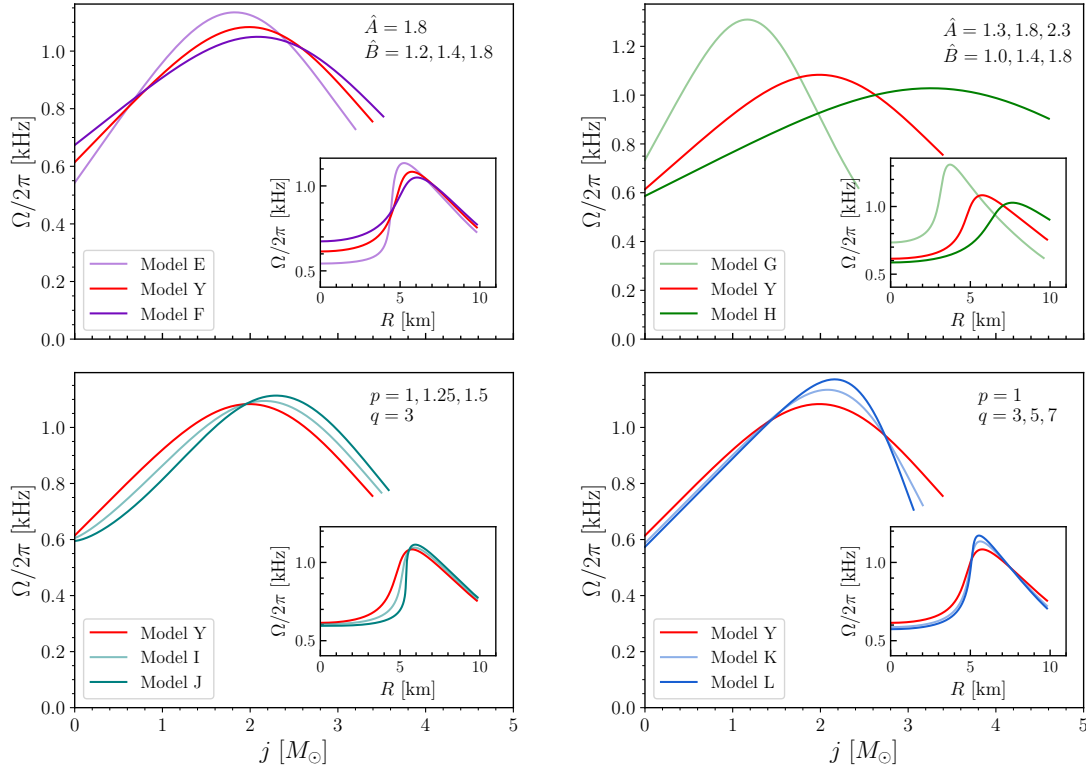


**Figure 3.** Angular velocity as a function of the specific angular momentum  $j$  for a stellar model obeying the DD2 EOS, having a central rest-mass density  $\rho_c = 8.024 \times 10^{14} \text{ g cm}^{-3}$ , and an axis ratio  $R_p/R_e = 0.8$ . The underlying differential rotation law is U8 and the different panels show how the functional form changes when varying the relevant parameters  $\hat{A}$ ,  $\hat{B}$ ,  $p$ ,  $q$  indicated in the top-right part of each panel. Note that each panel contains an inset reporting, for the same models, the angular velocity as a function of the proper circumferential radial coordinate  $R$ .

while the normalised maximum and equatorial angular velocities are expressed as

$$\lambda_1 := \frac{\Omega_{\max}}{\Omega_c} = \left(1 + \left(\frac{j_{\max}}{B^2 \Omega_c}\right)^p\right) \left(1 - \frac{j_{\max}}{A^2 \Omega_c}\right), \quad (34)$$

$$\lambda_2 := \frac{\Omega_e}{\Omega_c} = \left(1 + \left(\frac{j_e}{B^2 \Omega_c}\right)^p\right) \left(1 - \frac{j_e}{A^2 \Omega_c}\right). \quad (35)$$

After a bit of algebra, it is possible to show that the expressions for  $A$  and  $B$  appearing in (34) and (35) follow from the solution of the quadratic equation in  $B$

$$0 = B^4 \Omega_c^2 \left[ j_{\max}(1 - \lambda_2) - j_e(1 - \lambda_1) \right] + j_{\max}^{p+1} j_e^p - j_e^{p+1} j_{\max}^p + B^2 \Omega_c \left[ j_{\max} j_e^{p+1} (1 - \lambda_2) - j_e j_{\max}^p - j_e^{p+1} (1 - \lambda_1) \right]. \quad (36)$$

so that, after solving analytically for  $B$ , we can write an expression for  $A$  as

$$A^2 = \frac{1}{\Omega_c} \left[ \frac{j_{\max}(B^2 \Omega_c)^p + j_{\max}^{p+1}}{(B^2 \Omega_c)^p (1 - \lambda_1) + j_{\max}^p} \right] = \hat{A}^2 r_e^2. \quad (37)$$

As anticipated, the rotation integral (5) for the U9 law can be found analytically for arbitrary parameters  $p$ ,  $q$ .

$$\int_0^j j' \frac{d\Omega}{dj'} dj' = \Omega_c \left[ \frac{p}{p+1} \frac{j^{p+1}}{(B^2 \Omega_c)^p} - \frac{p}{p+2} \frac{j^{p+2}}{(B^2 \Omega_c)^p (A^2 \Omega_c)} - \frac{j^2}{2A^2 \Omega_c} - \frac{j^{p+2}}{p+2} \frac{1}{(B^2 \Omega_c)^p (A^2 \Omega_c)} \right], \quad (38)$$

while, in order to obtain the rotation frequency on the equatorial plane, we have to solve the Euler equation

$$0 = r_e^2 (\hat{\gamma}_e + \hat{\rho}_e - \hat{\gamma}_p - \hat{\rho}_p) + \ln \left[ 1 - (\hat{\Omega}_e - \hat{\omega}_e)^2 e^{-2r_e^2 \hat{\rho}_e} \right] + 2 \frac{\hat{\Omega}_e}{\lambda_2} \left[ \frac{p}{p+1} \frac{j_e^{p+1}}{(\hat{B}^2 \hat{\Omega}_e / \lambda_2)^p} - \frac{p}{p+2} \frac{j_e^{p+2}}{(\hat{B}^2 \hat{\Omega}_e / \lambda_2)^p (A^2 \hat{\Omega}_e / \lambda_2)} - \frac{j_e^2}{2\hat{A}^2 \hat{\Omega}_e / \lambda_2} - \frac{j_e^{p+2}}{p+2} \frac{1}{(\hat{B}^2 \hat{\Omega}_e / \lambda_2)^p (\hat{A}^2 \hat{\Omega}_e / \lambda_2)} \right], \quad (39)$$

with  $j_e$  as in Eq. (26), and then obtain the central rotational frequency  $\Omega_c = \Omega_e / \lambda_2$ .

We note that the numerical calculation of equilibrium models with the U9 law can lead to numerical challenges, at least with the Hydro-RNS code. In particular, convergence often fails at large values of  $\lambda_2$ , where  $\Omega_e > \Omega_c$ , as the iterated equatorial radius  $r_e$  alternates between two different solutions with different masses and radii for the same value of the axis ratio (these two branches merge again at small axis ratios). Considering that the branch yielding lower masses also exhibits an unphysical relation between the mass  $M$  and the specific angular momentum  $j$  (i.e.,  $M(j)$  is no longer injective with  $j$ ) and non-smooth profiles in  $\Omega(r)$  as well as  $M(j)$ , we consider such branch as “unphysical” and discuss hereafter only the results relative to the “physical” branch, that is, the branch yielding larger masses for the same axis ratio.

Examples of solutions with the U9 law are presented in the left panel of Fig. 4, which shows how the rotation profile changes with the parameter  $p$  at a fixed axis ratio of  $R_p/R_e = 0.8$  and a central rest-mass density of  $\rho_c = 8.024 \times 10^{14} \text{ g cm}^{-3}$ . Note how the variation of

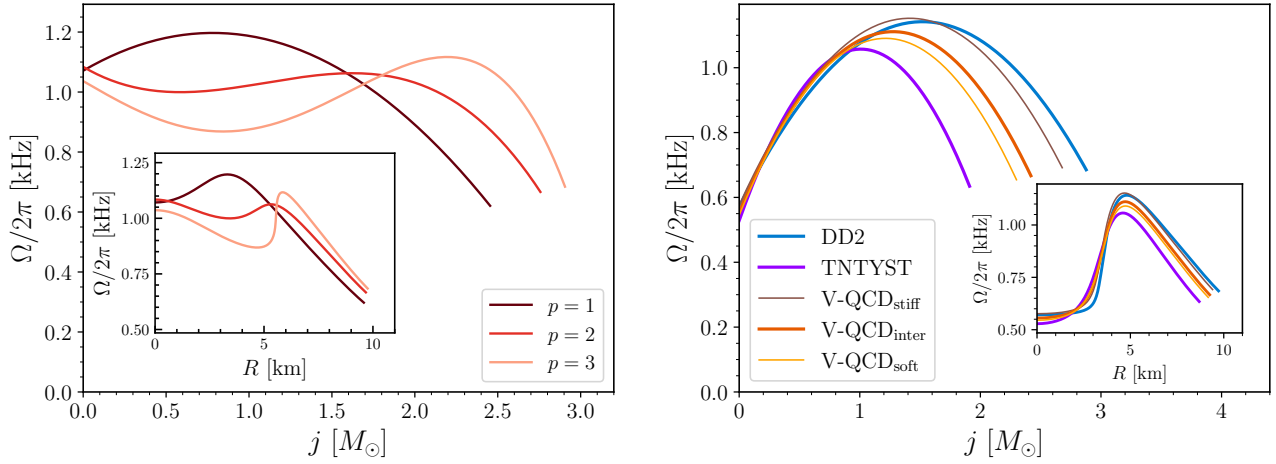


**Figure 4.** *Left panel:* the same as in Fig. 3 but with the U9 differential-rotation law when keeping fixed  $\hat{A} = 1.4$  and  $\hat{B} = 1$  and varying the exponent  $p = 1, 2, 3$ . *Right panel:* the same as in the left panel for  $p = 1$ ,  $\lambda_1 = 2$ ,  $\lambda_2 = 1.2$ . The various lines refer to the different EOSs: DD2 (blue), TNTYST (purple) and V-QCD with different degrees of stiffness (shades of orange). Also in this case, the insets in the panels offer a view of the angular velocity as a function of  $R$ .

the index  $p$  allows for considerably different functional behaviours of the rotation law and the appearance of an additional minimum which is seen for  $p = 2, 3$  (red and salmon lines). In essence, such values of the parameter  $p$  give rise to a region in the star which is rotating slower than both the center and the surface on the equatorial plane; while such a profile has not yet been observed in binary mergers, it may appear in the presence of phase transitions (Weih et al. 2020; Hanauske et al. 2021). Also seen in Fig. 4 is that the maximum in the angular velocity  $\Omega_{\max}$  shifts to larger radii and larger angular momenta. On the other hand, the impact of variations in the parameters  $\hat{A}$ ,  $\hat{B}$  or  $\lambda_1$ ,  $\lambda_2$  when using the U9 law is analogous to that discussed above for the U8 law and reported in Fig. 3.

The right panel of Fig. 4 offers some representative rotation profiles obtained with the U9 law for a fixed set of parameters, i.e.,  $p = 1$ ,  $q = 1$ ,  $\lambda_1 = 2$ ,  $\lambda_2 = 1.2$ ,  $\rho_c = 8.024 \times 10^{14} \text{ g cm}^{-3}$ ,  $R_p/R_e = 0.8$ , and different EOSs. Note that the angular-velocity profiles extends to larger values of angular momentum for stiffer EOSs, with the DD2 being the stiffest and the TNTYST (Togashi et al. 2017) the softest of the EOSs for such a value of the central rest-mass density [a similar behaviour is seen also for the V-QCD EOS (Jarvinen & Kiritsis 2012; Ishii et al. 2019; Ecker et al. 2020) in the three different cases considered].

We conclude the analysis of the U9 rotation law by considering the full space of solutions after setting  $p = 1$ ,  $q = 1$ ,  $\lambda_1 = 2$ ,  $\lambda_2 = 1.2$  (as in Fig. 5) and when considering the DD2 EOS. In analogy with Fig. 2, sequences of constant angular momentum are presented with a grey shading for  $J = 0.25, 0.5, \dots, 9.25$ , while the thick solid light-blue (blue) line shows the static case with  $\Omega = 0$  (the Keplerian limit of uniform rotation  $\Omega_{K,ur}$ ) and the green solid line indicates the stability line obtained with the turning point criterion.

Interestingly, the turning-point stability line crosses the Keplerian limit of uniform rotation exactly at its maximum  $M_{tp,K} = M_{\max,K,ur}$ , which is marked by a light blue square and terminates at the mass  $M = 3.34 M_\odot$ . Note also that the turning-point stability line has a negative slope, i.e., higher masses on the turning point line are at smaller central densities, in analogy with what we have seen in Fig. 2 for the U8 law and the DD2 EOS. As we will comment later on (see Sec. 5.2), this behaviour of the turning-point stability line is common but not the only one possible.

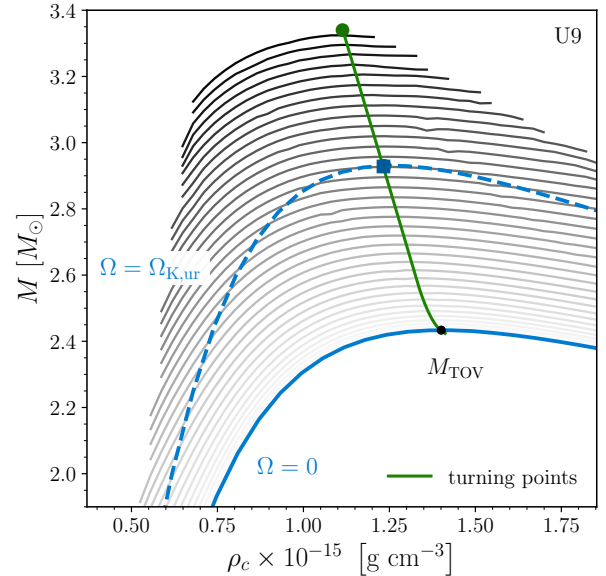


**Figure 5.** The same as in Fig. 2 but for the U9 differential-rotation law. Note that in this case the turning-point stability line (green solid line) intersects the Keplerian stability line at the maximum mass of Keplerian uniform-rotation models (blue filled square).

#### 4 DIFFERENTIAL-ROTATION LAWS FROM BNS MERGER SIMULATIONS

When building differentially rotating equilibria that are meant to model the HMNS produced in the merger of a binary system of neutron stars, it is clear that the only way to obtain *realistic* differential-rotation profiles it to extract this information from accurate and general-relativistic simulations of binary mergers using a state-of-the-art microphysical description. To this scope, we consider the results of BNS-merger simulations with three different temperature-dependent EOSs: DD2 (Hempel & Schaffner-Bielich 2010b), TNTYST (Togashi et al. 2017), and the V-QCD of intermediate stiffness (Demircik et al. 2020; Demircik et al. 2022).

More precisely, the first remnant we consider is the product of an equal-mass BNS with component masses  $M_{1,2} = 1.4 M_\odot$  evolved with the DD2 EOS by Ng et al. (2024); since it survives for times



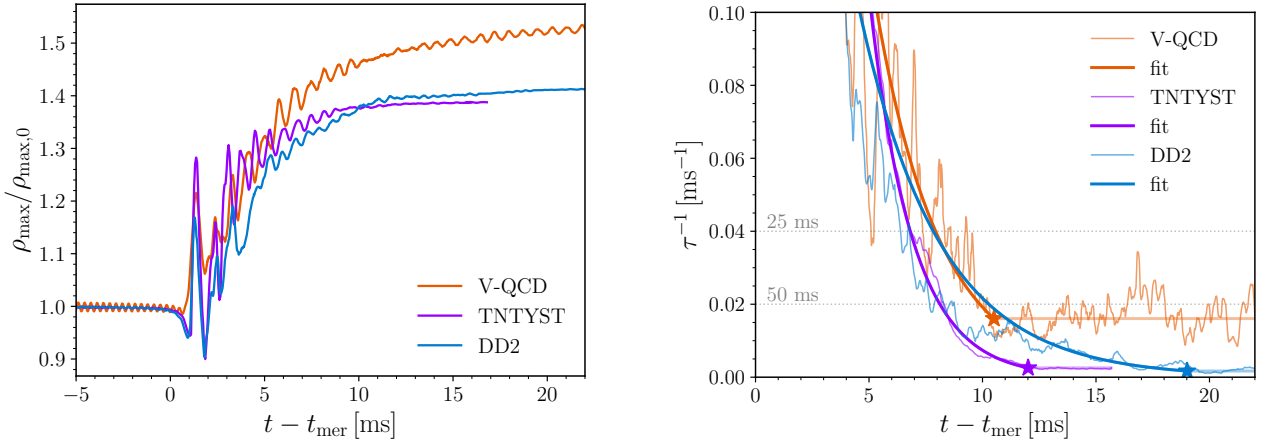


**Figure 6.** *Left panel:* evolution of the central rest-mass density normalised to its initial value for the DD2 (blue line), TNTYST (violet line) and V-QCD EOS (orange line). *Right panel:* evolution of the inverse of the equilibration timescale for the same EOSs as in the left panel. The bold lines represent the fit to the exponentially decaying part at early times and to the approximately constant part at later times. Grey dotted lines mark representative timescales.

$t - t_{\text{mer}} \gtrsim 100$  ms it represents a very good candidate to study how the properties and rotation profiles change with time and reach a quasi-stationary equilibrium. The second simulation considers the merger of a magnetized equal-mass binary with component masses  $M_{1,2} = 1.275 M_{\odot}$  and the TNTYST EOS (Togashi et al. 2017). In this case, a dipolar magnetic field is present inside the star with maximum magnetic-field strength  $B \sim 10^{14}$  G (Chabanov et al. 2023) and the merger remnant is an HMNS that does not collapse promptly to a black hole. Finally, the third merger remnant refers to an unequal-mass binary with mass ratio  $q := M_2/M_1 = 0.7$ , where  $M_1 = 1.64 M_{\odot}$  and  $M_2 = 1.15 M_{\odot}$ . The binary is evolved with the V-QCD EOS of intermediate stiffness, where the temperature dependence is introduced at low densities via the HS-DD2 EOS (including relativistic mean-field interactions) (Hempel & Schaffner-Bielich 2010a; Typel et al. 2010) and in the dense nuclear-matter phase via a van der Waals model (Demircik et al. 2022). In this case, the merger remnant has a lifetime of  $t - t_{\text{mer}} \gtrsim 37$  ms, which, as we will show below, is sufficient to extract robust rotation profiles. The basic properties of the binaries considered here and some of the corresponding dynamical properties have been summarised in Table 1.

#### 4.1 Expressions in the 3+1 decomposition

The simulations of BNS mergers are performed with the Einstein Toolkit (Loeffler et al. 2012; Haas & et al. 2020) within a 3+1 decomposition of spacetime, where the hydrodynamical variables and the metric coefficients are stored on a Cartesian grid on spacelike hypersurfaces (Rezzolla & Zanotti 2013). To extract the necessary information from the simulations output, we make use of the open-source post-processing tool Kuibit (Bozzola 2021), which is able to analyze different quantities from the Einstein Toolkit. However, since the simulation data is produced on a Cartesian grid while the equilibria are computed by RNS assuming a quasi-isotropic spherical coordinates system, a coordinate transformation is necessary to compute the angular velocity, the three-velocities and angular momentum in Cartesian coordinates.

More specifically, in the standard 3+1 decomposition of spacetime where  $\alpha$  is the lapse function,  $\beta$  the shift vector,  $\gamma$  the spatial part of the metric, and  $u$  the fluid four-velocity, we can compute the Lorentz

factor as

$$W := \alpha u^t = \frac{1}{\sqrt{1 - v^i v_i}}. \quad (40)$$

The expression for the angular velocity and for the angular momentum can be derived recalling that  $u_i = v_i \alpha u^t$ , so that the angular velocity is given by

$$\Omega := \frac{u^\phi}{u^t} = \alpha v^\phi - \beta^\phi, \quad (41)$$

while the specific angular momentum is

$$j := u^t u_\phi = u^t v_i \alpha u^t = \frac{W^2}{\alpha} v_\phi. \quad (42)$$

The corresponding quantities in Cartesian coordinates are instead given by

$$\Omega = \alpha \left( \frac{xv^y - yv^x}{x^2 + y^2} \right) - \frac{x\beta^y - y\beta^x}{\sqrt{x^2 + y^2}}, \quad (43)$$

and

$$j = \frac{W^2}{\alpha} \left[ \left( \frac{xv^y - yv^x}{x^2 + y^2} \right) \left( y^2 \gamma_{xx} - 2xy \gamma_{xy} + x^2 \gamma_{yy} \right) + \left( \frac{xv^x + yv^y}{\sqrt{x^2 + y^2}} \right) \left( \frac{yx}{\sqrt{x^2 + y^2}} \gamma_{xx} + \frac{y^2}{\sqrt{x^2 + y^2}} \gamma_{xy} - \frac{x^2}{\sqrt{x^2 + y^2}} \gamma_{yx} - \frac{xy}{\sqrt{x^2 + y^2}} \gamma_{yy} \right) + v^z \left( y \gamma_{xz} - x \gamma_{yz} \right) \right]. \quad (44)$$

#### 4.2 Quasi-stationarity and rotation profiles

For each of the simulations discussed above, we analyse the post-merger rotation profile of the long-living remnants, extracting rotation quantities such as the angular velocity  $\Omega$  and the specific angular momentum  $j$ . Furthermore, since the merger remnant has an equilibrium that varies rapidly right after the merger, attention needs to be paid to make sure that the rotational properties are measured when the remnant has reached a quasi-stationary equilibrium. To this scope,

**Table 1.** Properties of the BNS merger configurations. Reported are the initial masses  $M_1$ ,  $M_2$ , the EOS, and the collapse time  $t_{\text{coll}}$ . Also reported are the coefficients of the linear fit (47), the time  $t - t_{\text{mer}}$  at which is performed, and the corresponding values for the core radius  $R_{\text{core}}$ , the rest-mass density  $\rho_{\text{core}}$  and angular velocity  $\Omega_{\text{core}}$  of the core.

EOS	$M_1$ [ $M_\odot$ ]	$M_2$ [ $M_\odot$ ]	$t_{\text{coll}}$ [ms]	$t - t_{\text{mer}}$ [ms]	$a \times 10^{-2}$ [kHz]	$b$ [kHz]	$\rho_{\text{core}} \times 10^{-13}$ [g cm $^{-3}$ ]	$\Omega_{\text{core}}/2\pi$ [kHz]	$R_{\text{core}}$ [km]
DD2	1.400	1.400	> 100	20	1.480	2.456	5.963	1.088	11.982
TNTYST	1.275	1.275	> 20	13	1.957	3.086	3.355	1.157	11.129
V-QCD	1.640	1.150	> 37	12	2.038	3.084	2.911	1.060	12.023

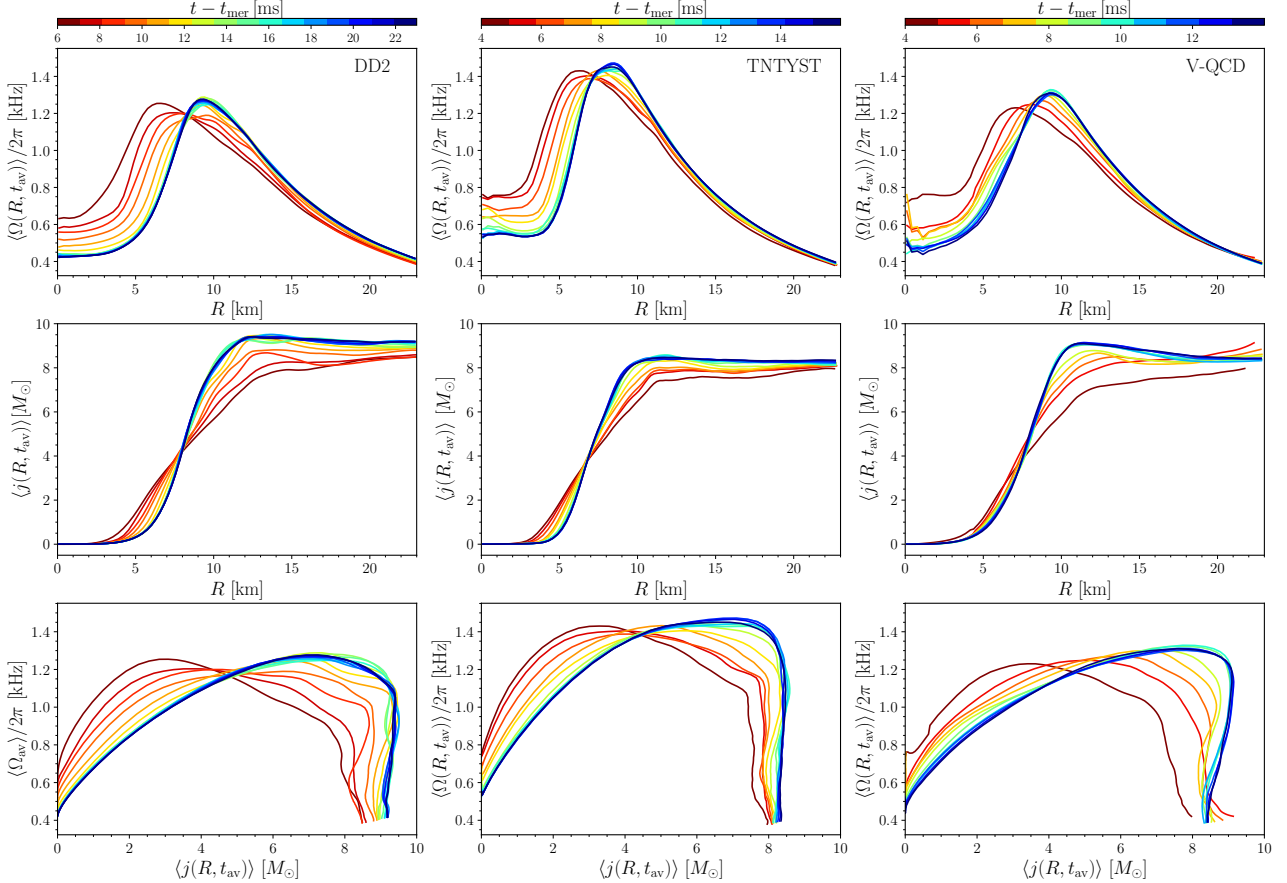


**Figure 7.** Evolution of the rotational properties of the BNS merger remnant obtained with the DD2 EOS (left column), the TNTYST EOS (middle column) and the V-QCD EOS (right column). In each panel, coloured lines following the colourmap at the top show the different profiles as measured at different average times  $t_{\text{av}}$  after the merger with a cadence of 1 ms. From top to bottom, the different rows show the angular velocities and the specific angular momentum as a function of  $R$ , as well as the angular velocity as a function of  $j$  for the three EOSs. All quantities show are averaged in azimuthal angle and time (see also Fig. A1 for a higher cadence).

we define a time window after the merger with extremes  $t - t_{\text{mer}} = t_1$  and  $t - t_{\text{mer}} = t_2$  (where  $0 < t_1 < t_2$ ) during which we monitor the evolution of properties of the merger remnant. In particular, we use  $t_1$  as a reference time from when the system has started to reach a quasi axisymmetric equilibrium and  $t_2$  to mark the time when this equilibrium has been reached to a given tolerance.

More specifically, while any hydrodynamical quantity could be employed to this scope, we take the evolution of the maximum rest-mass density of the merger remnant normalised to the initial value as a good proxy for the measurement of  $t_1$  and  $t_2$ . The left panel of Fig. 6 reports the evolution of this quantity for the three EOSs considered here and represented with a colorcode that we will employ hereafter, and clearly shows that while the inspiral is characterised

by an almost-constant behaviour in time, the merger is marked by a large increase accompanied by large-amplitudes oscillations that are gradually damped in time, thus leading to a new, almost-constant behaviour. Using this information, we can define an “equilibration timescale”  $\tau := \rho_{\text{max}}(t)/\dot{\rho}_{\text{max}}(t)$ , with a dot indicating a time derivative, and whose evolution is shown in the right panel of Fig. 6. While this timescale has high-frequency oscillations (thin solid lines), it also exhibits a clear exponential-decay behaviour from  $t - t_{\text{mer}} = t_1$  that we capture with a fit of the type  $\ln(\tau) = m(t - t_{\text{mer}}) + b$  with slope  $m < 0$  (thick solid lines). The exponential decay is followed by an evolution in which  $\tau \simeq \text{const.}$  and we use the transition between the exponential decay and the constant-in-time evolution to mark  $t - t_{\text{mer}} = t_2$  (these times are shown with filled stars in Fig. 6). As a

result, the corresponding values for the three remnants are

- DD2 :  $t_1 = 6$  ms,  $t_2 = 19.0$  ms,
- TNTYST :  $t_1 = 4$  ms,  $t_2 = 12.0$  ms,
- V-QCD :  $t_1 = 4$  ms,  $t_2 = 10.5$  ms.

Note in the right panel of Fig. 6 that the equilibration timescales are different for the various EOSs and that  $\tau$  reaches a constant value rather rapidly for the V-QCD EOS, but also that this value is larger than for the other two (dotted grey lines report the corresponding values of the equilibration timescale in milliseconds). This is also reflected in the left panel of Fig. 6, where the corresponding normalised rest-mass density continues to maintain small oscillations as a result of the original mass asymmetry in the binary. Similarly, note that even though the remnant of the DD2 merger has the largest equilibration timescale, it reaches it only at a comparatively later time.

Having defined the window in time where it is interesting to study the evolution of the rotational properties of the merger remnant, we introduce azimuthal and time-averaged representation of the angular velocity and of the specific angular momentum, namely,

$$\langle \Omega(R, t_{av}) \rangle := \frac{1}{2\pi\Delta t} \int_0^{2\pi} \int_{t_{av}-\Delta t/2}^{t_{av}+\Delta t/2} \Omega(R, \phi, t) d\phi dt, \quad (45)$$

$$\langle j(R, t_{av}) \rangle := \frac{1}{2\pi\Delta t} \int_0^{2\pi} \int_{t_{av}-\Delta t/2}^{t_{av}+\Delta t/2} j(R, \phi, t) d\phi dt. \quad (46)$$

where we set  $\Delta t = 1$  ms and the averaging window is taken to vary in the interval  $t_1 < t_{av} < t_2$ . Using these averaged quantities (45) and (46), it is possible to study the behaviour of the rotation profiles  $\Omega(j)$  and how they change from soon after the merger (i.e.,  $t_{av} \simeq t_1$ ) to the time when the HMNS has reached a quasi-stationary equilibrium (i.e.,  $t_{av} \simeq t_2$ ).

Figure 7 presents the evolution of  $\langle \Omega \rangle$  (top row) and  $\langle j \rangle$  (bottom row) shown as a function of the proper radius  $R$  for the remnants with three different EOSs (different columns) and with the averaging time  $t_{av}$  having a cadence of 1 ms as being indicated by the colormap going from  $t_1$  (red) to  $t_2$  (blue; Fig. A1 in Appendix A offers a similar evolution for the DD2 EOS where  $t_{av}$  is chosen across the interval  $5 \text{ ms} < t - t_{mer} < 23 \text{ ms}$  but with a finer time interval, i.e.,  $\Delta t = 0.1$  ms.)

Clearly, a very similar behaviour is shown by all remnants in Fig. 7, with only minor differences related to the EOS and the mass ratio. In particular, at early times  $t_{av} \gtrsim t_1$  (red lines) the angular velocities have maxima  $\Omega_{max}$  which are larger than at later times and are positioned closer to the center (top row); the angular profile is essentially Keplerian outside the maximum and can be associated to the low rest-mass density “disc” around the HMNS (Kastaun & Galeazzi 2015; Hanauske et al. 2017); a similar behaviour has been seen also in the actual discs produced when the HMNS collapses to a BH (see, e.g., Rezzolla et al. 2010). Hence, the position of the maximum of the angular velocity can be taken as to mark the “outer edge” of the HMNS and the “inner edge” of the disc surrounding it. Between  $t_1$  and  $t_2$ , the maxima move to smaller values of the angular velocity and outwards from the center (yellow and green lines). At late times,  $t_{av} \lesssim t_2$  (blue lines), the changes in time are much smaller and the maxima in the angular velocities attain their equilibrium values and positions. Importantly, note that the “core” of the HMNS is rotating almost uniformly and it slows down and grows in size between  $t_1$  and  $t_2$  for all the binaries considered, reaching a size of  $\approx 5$  km (see also Kastaun & Galeazzi 2015; Hanauske et al. 2017).

A similar behaviour is shown also by the specific angular momentum (middle row), which is however monotonic and joins two

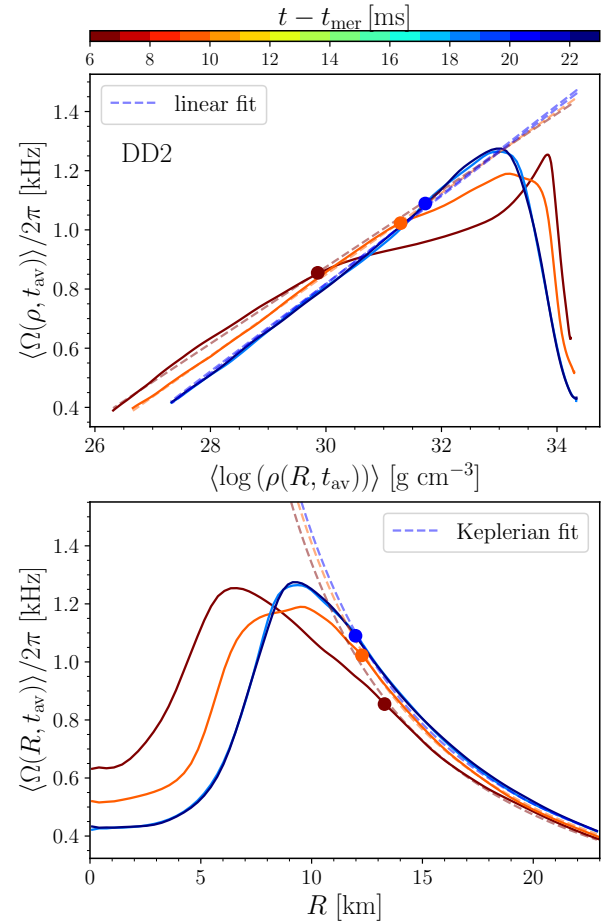


**Figure 8.** *Top panel:* angular velocity as a function of the logarithm of the rest-mass density for the BNS remnant modeled with the DD2 EOS at three different averaging times after the merger  $t_{av} = 6, 9, 18, 22$  ms (see colormap on the top). Indicated with dashed lines are the linear fits and marked with coloured filled circles are the locations of the departures from a linear behaviour. *Bottom panel:* the same as in the top panel but when the angular velocity is shown as a function of  $R$ . The dashed lines reproduce the Keplerian fall-off of  $R^{-3/2}$  and it should be noted that the fit is starts to be valid from the position of the three filled circles, which can therefore be taken to distinguish the core from the disc in the HMNS.

almost-constant states in the core of the HMNS and in its disc. Unsurprisingly, the presence of a uniformly-rotating core in the HMNS is clear also in terms of the specific angular momentum, which is very constant and close to zero, and whose size increases with time reaching the quasi-stationary size of  $\approx 5$  km. Note also that as time progresses the specific angular momentum in the HMNS interior (not only in the core) decreases, while it increases outside and in the HMNS disc; this happens at  $R \approx 10$  km. A slight deviation from the behaviour described above is seen for the V-QCD EOS but we attribute this mostly to the fact that the data refers to a binary with a considerable difference in mass and for which the disc may reach a constant state on longer timescales than those considered here.

Finally, the bottom row of Fig. 7 presents the evolution of  $\langle \Omega \rangle$  as a function of  $\langle j \rangle$ , i.e.,  $\langle \Omega \rangle(\langle j \rangle)$ , which is instructive, since this is the quantity that needs to be integrated to compute the first integral of the hydrostationary equilibrium [see Eq. (11)]. Obviously, this quantity combines the behaviours discussed in the top and middle row and reflects how, from  $t_1$  to  $t_2$ , the decrease of specific angular momentum leads to a decrease of  $\langle \Omega \rangle(\langle j \rangle)$  in the HMNS interior

and to a corresponding increase in the exterior, as expected from a rough conservation of angular-momentum (we recall that angular momentum within the HMNS is not perfectly conserved as it is radiated via GWs and lost in part via shocks). In the following sections we will use the numerical profiles of  $\langle\Omega\rangle(\langle j\rangle)$  at  $t_2$  to construct realistic equilibrium models of differentially rotating stars.

### 4.3 Distinguishing core and disc in the remnant

A problem frequently arising when modelling an HMNS is to distinguish the actual “core” from what is normally referred as “disc”. This distinction is often made in terms of cut-off densities, e.g.,  $10^{13}$  g/cm<sup>3</sup>. While this choice is reasonable, it is fundamentally arbitrary and any other cut-off density could be chosen in principle, hence leading to different results.

To counter this arbitrariness and define a criterion that is grounded on the physical properties of the HMNS once a quasi-stationary configuration has been reached, we have investigated the functional dependence of the remnant’s angular velocity as a function of the rest-mass density at different times after the merger. This is shown in the top panel Fig. 8, where we report the azimuthally averaged and over a 1 ms-window averaged angular-velocity profiles as a function of the logarithm of the averaged (in time and azimuth) rest-mass density for the DD2 EOS and at four different times, i.e.,  $t - t_{\text{mer}} = 6, 9, 18$  and 22 ms (brown, orange, light-blue, and dark-blue, respectively; note that the last lines are essentially overlapping because of the attained quasi-stationarity). Note the interesting linear behaviour of  $\Omega = \Omega(\log(\rho))$ , which can be effectively fitted with a simple function of the type

$$\Omega(\rho) = a \log(\rho) + b, \quad (47)$$

with parameters  $a$  and  $b$  that are functions of time and are reported in Table 1. Since the linear (in log) fitting works well for the low-density regions of the disc but fails as the densities increase and the core is approached, we exploit the change of behaviour to mark the transition between the disc and the core. This is shown with filled circles, whose positions vary in time and highlight that the core in the HMNS actually “shrinks” over time but soon settles to a quasi-stationary value. Obviously, as the core shrinks, the inner position of the disc also decreases, as can be appreciated from the bottom panel of Fig. 8, which reports the angular-velocity profile as a (linear) function of the radius and where the filled circles are the same as in the top panel.

A few remarks are worth making. First, note that the point of departure from a linear-in-log behaviour of the angular velocity with the rest-mass density coincides with the corresponding departure of the angular velocity from a Keplerian profile with radius. This is not surprising but underlines that the point of departure can be interpreted either as the “beginning” of the Keplerian disc, i.e.,  $R_{\text{core}}$  or as the “end” location of where the density in the HMNS stops growing as a power-law with radius, i.e.,  $\rho_{\text{core}}$ . Second, note that the “core-disc” transition does not coincide with the maximum of the angular velocity, which systematically lies at smaller radii; this point, which was already remarked by [Hanauske et al. \(2017\)](#), warns against using the angular velocity maximum as a particularly significant location in the HMNS. Third, note that at least in the limited sample considered here  $\rho_{\text{core}}$  varies by a factor two at most, i.e., between  $\approx 3 \times 10^{13}$  g/cm<sup>3</sup> and  $\approx 6 \times 10^{13}$  g/cm<sup>3</sup> (see Table 1). Finally, note that  $R_{\text{core}}$  has a much smaller variance (i.e.,  $\lesssim 7\%$ ) and while a more systematic analysis may constrain this value more precisely, it is interesting that very different binaries lead to essentially the same core radius.

All things considered, the suggestion of determining the start of the disc as the location where the angular velocity does no longer follow a power-law with the rest-mass density appears to be easy to employ and physically well-grounded; furthermore it points out that values  $\rho_{\text{core}} \approx 4 \times 10^{13}$  g/cm<sup>3</sup> and  $R_{\text{core}} \approx 12$  km can be taken as a reasonable references for the core density and radius, respectively.

## 5 NEW AND REALISTIC DIFFERENTIAL-ROTATION LAWS

Having discussed in detail in the previous section the laws of differential rotation that are actually measured from BNS merger simulations, we note that the traditional prescriptions to model differential rotation laws presented in Sec. 3 generically offer difficulties in generating stellar models that have, at the same time, large radii and large angular-velocity maxima. This motivates us to seek new differential rotation laws that are either extensions of the Uryu laws (Sec. 5.1) or novel formulations (Sec. 5.2), and that provide a very accurate description of what is measured from fully nonlinear simulations. In what follows, we discuss such new differential-rotation laws and their properties.

### 5.1 The extended Uryu-9 rotation law

The simplest way to produce a differential-rotation law that provides a better match with the results of the simulations is to “extend” the U9 law via the introduction of a new exponent  $\xi$  whose role is to increase the magnitude of the angular-velocity maximum, so that expression (31) can now be written as

$$\Omega(j) = \Omega_c \left( 1 + \left( \frac{j}{B^2 \Omega_c} \right)^p \right) \left( 1 - \left( \frac{j}{A^2 \Omega_c} \right)^\xi \right). \quad (48)$$

such that  $\xi = 1$  yields the standard U9 law and  $\xi \neq 1$  leads to the extended U9 law, or “U9+” hereafter. Also in this case, it is possible to compute analytically the first and second-order derivatives of  $\Omega(j)$  with respect to the specific angular momentum and obtain respectively

$$\begin{aligned} \frac{d\Omega}{dj} &= \Omega_c \left[ p \frac{j^{p-1}}{(B^2 \Omega_c)^p} \left( 1 - \left( \frac{j}{A^2 \Omega_c} \right)^\xi \right) \right. \\ &\quad \left. - \xi \frac{j^{\xi-1}}{(A^2 \Omega_c)^\xi} \left( 1 + \left( \frac{j}{B^2 \Omega_c} \right)^p \right) \right], \end{aligned} \quad (49)$$

and

$$\begin{aligned} \frac{d^2\Omega}{dj^2} &= \Omega_c \left[ p(p-1) \frac{j^{p-2}}{(B^2 \Omega_c)^p} \left( 1 - \left( \frac{j}{A^2 \Omega_c} \right)^\xi \right) \right. \\ &\quad - p \frac{j^{p-1}}{(B^2 \Omega_c)^p} \xi \frac{j^{\xi-1}}{(j/(A^2 \Omega_c))^\xi} - p \frac{j^{p-1}}{(B^2 \Omega_c)^p} \left( \xi \frac{j^{\xi-1}}{(A^2 \Omega_c)^\xi} \right) \\ &\quad \left. - \left( 1 + \left( \frac{j}{B^2 \Omega_c} \right)^p \right) \frac{\xi(\xi-1)j^{\xi-2}}{(j/(A^2 \Omega_c))^\xi} \right]. \end{aligned}$$

In this case, the rotation integral is given by

$$\begin{aligned} \int j' \frac{d\Omega}{dj'} dj' &= \\ \Omega_c \left[ \frac{p}{p+1} \frac{j^{p+1}}{(B^2 \Omega_c)^p} - \frac{p}{p+\xi+1} \frac{j^{p+\xi+1}}{(B^2 \Omega_c)^p (A^2 \Omega_c)^\xi} \right] \end{aligned}$$



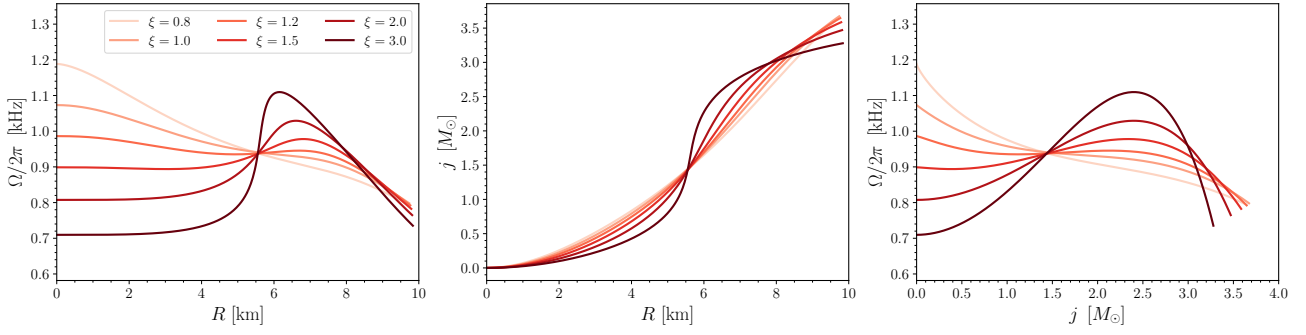


**Figure 9.** Rotational properties of stellar models obeying the U9+ differential-rotation law. From left to right we show the radial profiles of the angular velocity (left panel), the radial profile of the specific angular momentum (middle panel) and the angular velocity as a function of the specific angular momentum (right panel). The different curves are obtained when keeping fixed the parameters  $p = 2$ ,  $\hat{A} = 1.8$ ,  $\hat{B} = 1.4$  and varying the exponent  $\xi \in [0.6, 3]$ ; also in this case, the stellar model obeys the DD2 EOS, has a central rest-mass density  $\rho_c = 8.024 \times 10^{14} \text{ g cm}^{-3}$ , and an axis ratio  $R_p/R_e = 0.8$ .

$$-\frac{\xi}{\xi+1} \frac{j^{\xi+1}}{(A^2 \Omega_c)^\xi} - \frac{\xi}{p+\xi+1} \frac{j^{p+\xi+1}}{(B^2 \Omega_c)^p (A^2 \Omega_c)^\xi} \Bigg]. \quad (50)$$

and, as for the U9 law, we can compute  $B$  from the solution of the quadratic equation

$$0 = B^{2p} \Omega_c^p \left\{ B^{2p} \Omega_c^p \left[ j_{\max}^\xi (1 - \lambda_2) - j_e^\xi (1 - \lambda_1) \right] + j_{\max}^{p+\xi} (1 - \lambda_2) - j_e^\xi j_{\max}^p + j_e^p j_{\max}^\xi - j_e^{p+\xi} (1 - \lambda_1) \right\} - j_{\max}^{p+\xi} j_e^p - j_e^{p+\xi} j_{\max}^p. \quad (51)$$

so that, again, after solving analytically for  $B$ , we can write an expression for  $A$  as

$$A^2 = \frac{1}{\Omega_c} \left( \frac{-(B^2 \Omega_c)^p F_{\max}^\xi - j_{\max}^{p+\xi}}{(\lambda_1 - 1)(B^2 \Omega_c)^p - j_{\max}^p} \right)^{\frac{1}{\xi}}. \quad (52)$$

In Fig. 9 we report some representative U9+ solutions obtained for stars modeled with the DD2 EOS with a fixed central rest-mass density of  $\rho_c = 8.024 \times 10^{14} \text{ g cm}^{-3}$  and an axis ratio of  $R_p/R_e = 0.8$ . The different curves refer to different values of the exponent  $\xi$ , while the other parameters in the U9+ law, namely,  $\hat{A} = 2.5$ ,  $\hat{B} = 1.8$ ,  $p = 2$ , are kept fixed. As seen from the left and right panels, values  $\xi < 3$  tend to change the values of the angular velocity at the center and beginning of the disc. In particular, for  $\xi < 1.2$  the angular-momentum maximum is reached at the center of the star, and for  $\xi < 1.0$  the angular-velocity essentially decreases monotonically with radius, thus behaving in a way that is similar to the  $j$ -constant law.

An interesting feature that emerges from the use of the U9+ law, although it is not peculiar of this law, can be appreciated from Fig. 10, which reports the usual sequences of constant angular momentum  $J$  for models with the DD2 EOS and the following set of parameters:  $p = 0.8$ ,  $\xi = 3$ ,  $\lambda_1 = 3$ ,  $\lambda_2 = 2.8$ . Also shown in Fig. 10 is the standard stability line obtained by joining the various turning points. When comparing with the corresponding Figs. 2 and 5 is it quite apparent that the turning-point stability line (orange solid line) has a positive slope, i.e., that  $\partial M / \partial \rho_c|_{\text{tp}} > 0$ , thus in stark contrast with what is seen for the space of solutions with the U8 and U9 differential-rotation laws. The most important consequence of this behaviour is that it is in principle possible to construct two stellar models located on the Keplerian stability line that have the same gravitational mass but different central rest-mass densities, and obviously different internal structure. We postpone a more detailed discussion of what these differences in the stellar structure amount to until Sec. 5.3,

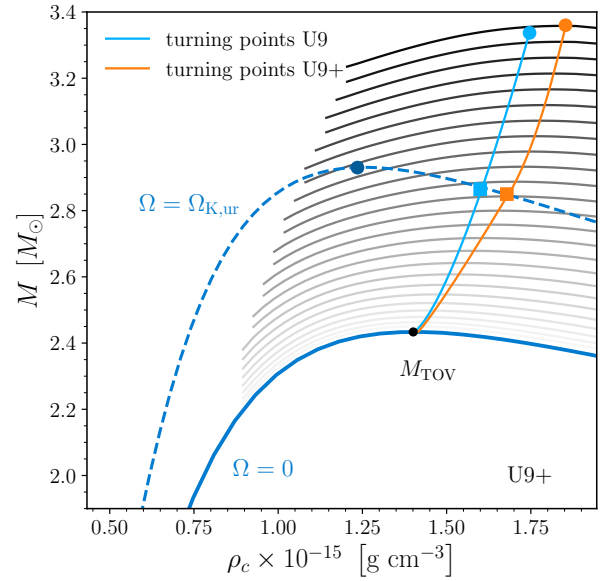


**Figure 10.** The same as in Fig. 2, but for the new U9+ differential-rotation law (orange line) and for a different parameterisation of the U9 law (light-blue line; see also Fig. 5). Note that for these rotation laws, the turning-point stability line has a positive slope (see also Fig. 10)

where we will be able to discuss them from a more general point of view and when considering also other rotation laws. However, it can suffice here to say that this novel behaviour of the turning-point critical line is not unique nor an intrinsic property of the U9+ rotation law. Indeed, it is possible to reproduce a very similar behaviour for the same DD2 EOS also for the U9 law once the following parameters are carefully chosen:  $p = 1$ ,  $\lambda_1 = 3$ ,  $\lambda_2 = 2.8$ . The corresponding turning-point stability line is shown in Fig. 10 (light blue solid line)<sup>1</sup> and thus highlights that constructing differentially rotating models whose maximum mass at constant angular momentum increases with central density is more common than one may naively assume.

<sup>1</sup> Note that for clarity we do not show in Fig. 10 the constant- $J$  sequences for the U9 law, which are obviously different from those of the U9+ law.

### 5.2 A new differential-rotation law

As we will discuss in more detail in Sec. 5.3, the added flexibility introduced in the U9+ law allows it to provide a rather accurate description of realistic differential-rotation profiles measured from BNS mergers. At the same time, it can be further improved via a novel differential-rotation law that is directly informed from the simulations and there the angular velocity can be modeled as

$$\Omega(j) = \begin{cases} \Omega_c \left[ \lambda_1 - (\lambda_1 - 1) (1 - j/j_{\max})^{2\beta} \right], & j < j_{\max} \\ \Omega_c \lambda_1 - \Omega_c \lambda_1 (j/j_{\max} - 1)^{2\gamma} A, & j \geq j_{\max} \end{cases},$$

Because the first derivative is simply given by

$$\frac{d\Omega(j)}{dj} = \begin{cases} 2\beta\Omega_c(\lambda_1 - 1)/j_{\max} (1 - j/j_{\max})^{2\beta-1}, & j < j_{\max} \\ 2\gamma\Omega_c\lambda_1/j_{\max} (j/j_{\max} - 1)^{2\gamma-1} A, & j \geq j_{\max} \end{cases} \quad (53)$$

the associated rotation integral has an analytical expression for the rotation integral and varies whether  $j \leq j_{\max}$  or  $j > j_{\max}$ . In the former case, the integral is given by

$$j_{\max}\Omega_c(\lambda_1 - 1) \left[ 1 - \left(1 - \frac{j}{j_{\max}}\right)^{2\beta} - \frac{2\beta}{2\beta + 1} \left(1 - \left(1 - \frac{j}{j_{\max}}\right)^{2\beta+1}\right) \right], \quad (54)$$

while in the latter case it has the more complex expression

$$j_{\max}\Omega_c(\lambda_1 - 1) \left\{ \left(1 - \frac{2\beta}{2\beta + 1}\right) - 2A\gamma \left[ \frac{1}{2\gamma + 1} \left(1 - \frac{j}{j_{\max}}\right)^{2\gamma+1} - \frac{1}{2\gamma} \left(1 - \frac{j}{j_{\max}}\right)^{2\gamma} \right] \right\}. \quad (55)$$

Note that when implementing the rotation law (53) in the Hydro-RNS code we need to introduce the standard (rescaled) parameters  $\hat{j}_{\max}$ ,  $\hat{j}_e$ ,  $\lambda_1$ ,  $\lambda_2$ , and  $A$ , but also the new parameters  $\beta$  and  $\gamma$ . We postpone to Sec. 5.3 the discussion of how the new differential-rotation law – that hereafter will refer to as the “CR” law – performs when modelling the remnants of BNS mergers, we here briefly provide evidence that this law allows one to construct numerical models of differentially rotating stars by presenting in Fig. 11 a representative space of solutions for stars modelled with the DD2 EOS and with the following set of fixed parameters:  $\hat{j}_{\max}/\hat{j}_e = 0.82$ ,  $\beta = 0.95$ ,  $\gamma = 1.8$ ,  $A = 20$ ,  $\lambda_1 = 3$  and that was obtained after performing a progressive linear blending with the U9+ law, as discussed in Appendix B. Note that also in this case, the choice of parameters leads to a turning-point stability line such that  $\partial M/\partial \rho_c|_{\text{tp}} > 0$ . As we comment next, this is not a coincidence and reflects a general behaviour of differential-rotation laws that are inspired by BNS mergers.

### 5.3 Comparison of various differential-rotation laws

After having reviewed the traditional differential-rotation laws (and their extensions) and discussed how new laws can be introduced and solved numerically, it is now useful to actually compare and contrast the different laws against some representative differential-rotation as deduced from fully nonlinear simulations. We do this by considering the BNS merger computed with the DD2 EOS and whose differential-rotation profile has been extracted at  $t - t_{\text{mer}} = 20$  ms (see Fig. A1 in Appendix A), which we reproduce using three different laws: U9, U9+ and CR. In all cases, we consider models with a

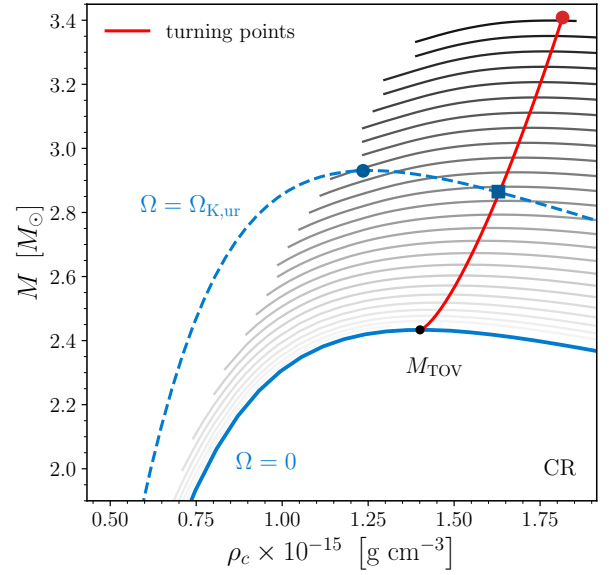


**Figure 11.** The same as in Fig. 2, but for the new CR differential-rotation law; note that also in this case, the turning-point stability line has a positive slope (see also Fig. 10).

central rest-mass density  $\rho_c = 8.024 \times 10^{14} \text{ g cm}^{-3}$  and an axis ratio  $R_p/R_e = 0.7$ . In addition, for the U9 (U9+) laws we use respectively the following set of parameters  $p = 1$ ,  $\lambda_1 = 3$ ,  $\lambda_2 = 2.8$  ( $p = 0.8$ ,  $\xi = 3$ ,  $\lambda_1 = 3$ ,  $\lambda_2 = 2.8$ ), which have been chosen so as to optimise the match with the numerical data. The stellar model following the CR law, on the other hand, has been obtained after fixing  $j_{\max}/j_e = 0.82$ ,  $\beta = 0.95$ ,  $\gamma = 1.8$ ,  $A = 20$ , and  $\lambda_1 = 3$ <sup>2</sup>.

A summary of the comparison of the data is offered in Fig. 12, which reports the remnant profiles from the simulations (dark-blue lines) and the corresponding matches with the U9 (light-blue lines), the U9+ law (orange lines), and the CR law (red lines). As in previous figures, the different panels offer views of  $\Omega = \Omega(R)$  (left panel),  $j = j(R)$  (middle panel), and  $\Omega = \Omega(j)$  (right panel). Note that for all the three different fitting laws we show with solid (dashed) lines the profiles computed by Hydro-RNS inside (outside) the stellar model. Also reported at the bottom of each panel is the relative difference of the given quantity  $\phi$  between the numerical-relativity data and the corresponding fitting law, i.e.,  $|\delta| := |1 - \phi_{\text{BNS}}/\phi_{\text{fit}}|$ . Overall, the comparison performed in Fig. 12 indicates that all of the rotation laws provide a very good match with the data, but also that the ability to adjust the  $\xi$  exponent in the U9+ law allows the latter to achieve a closer representation of the BNS merger data. However, both the U9 and the U9+ laws, provide rather inaccurate representations of the data in the portion of the solution that we have considered to be the disc and that is indicated with dashed light-blue and orange lines, respectively. The CR law, on the other hand, provides a more accurate representation of the numerical data both in the central parts of the merger remnant and of the corresponding

<sup>2</sup> Obviously, a similarly good fit can be obtained also for the TNTYST EOS at  $t - t_{\text{mer}} = 13$  ms. For completeness, and to aid reproducibility, we list below the best-fit parameters. For the U9 (U9+) law, the relevant parameters are  $p = 1$ ,  $\lambda_1 = 2.7$ ,  $\lambda_2 = 2.5$  ( $p = 0.8$ ,  $\xi = 2.5$ ,  $\lambda_1 = 2.7$ ,  $\lambda_2 = 2.5$ ). Similarly, for the CR law they are  $j_{\max}/j_e = 0.84$ ,  $\beta = 1.12$ ,  $\gamma = 2.1$ ,  $A = 90$ , and  $\lambda_1 = 2.7$ . The best-matching models computed with Hydro-RNS have a central rest-mass density of  $\rho_c = 1.074 \times 10^{15} \text{ g cm}^{-3}$  and an axis ratio of  $R_p/R_e = 0.68$ .

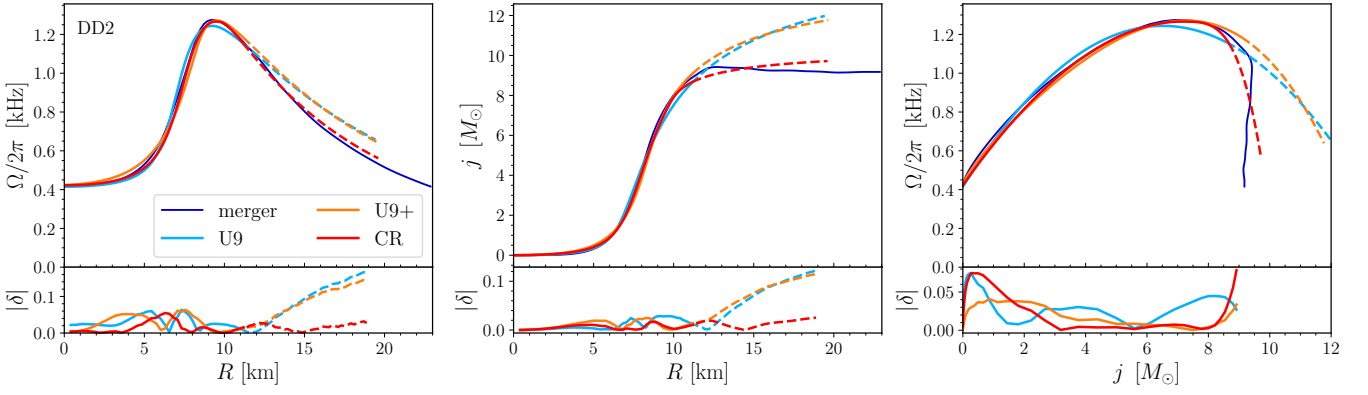


**Figure 12.** Comparison of the rotational properties of a BNS merger remnant with different laws of differential rotation. From left to right we show the radial profiles of the angular velocity (left panel), the radial profile of the specific angular momentum (middle panel) and the angular velocity as a function of the specific angular momentum (right panel). Shown with blue lines are the data from the numerical simulations at  $t - t_{\text{mer}} = 20$  ms, while lines of other colours show the behaviour of the various laws: light blue for U9, orange for U9+, and red for CR. Note that for these laws, the transition from solid to dashed lines refers to transition from the core to the disc or, equivalently, from a numerical to an analytic solution.

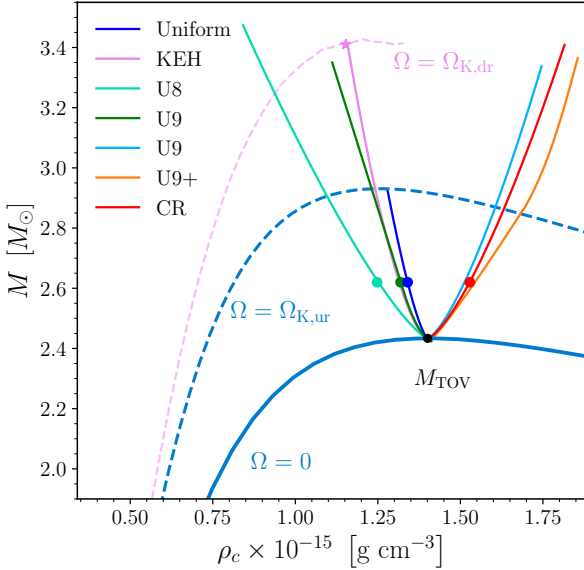


**Figure 13.** The same as in Fig. 2, but for all of the differential-rotation laws considered here:  $j$ -constant law (violet line), U9 law (green and light-blue lines), the U9+ law (orange line) and the new CR law (red line); see also Figs. 5, 10, and 11. The Keplerian limit of differentially rotating models obeying the  $j$ -constant law for  $\hat{A} = 3.33$ , i.e.,  $\Omega = \Omega_{K,dr}$ , is shown with a pink dashed line; the solid filled circles mark the stellar models shown in Fig. 15.

disc, with a relative error that remains  $|\delta| \lesssim 5\%$  (for  $\phi = \Omega(R)$  and  $\phi = \Omega(j)$ ). While this better match is also the result of the more complex functional structure of the CR law, the fact that its solution is not computationally more challenging than that of the U9 or the U9+ laws, makes the newly proposed CR differential-rotation law a potentially optimal description of the properties of the post-merger remnants from BNS simulations.

We conclude this section by returning to a topic already covered in the previous sections, namely that of the turning-point stability line, but that we here discuss in a more comprehensive way and collecting all the differential-rotation laws we have considered in this work. Figure 13 offers in a single plot a complete view of the turning-point stability lines for the various laws considered so far and referred to stellar models obeying a DD2 EOS. As in previous versions of this

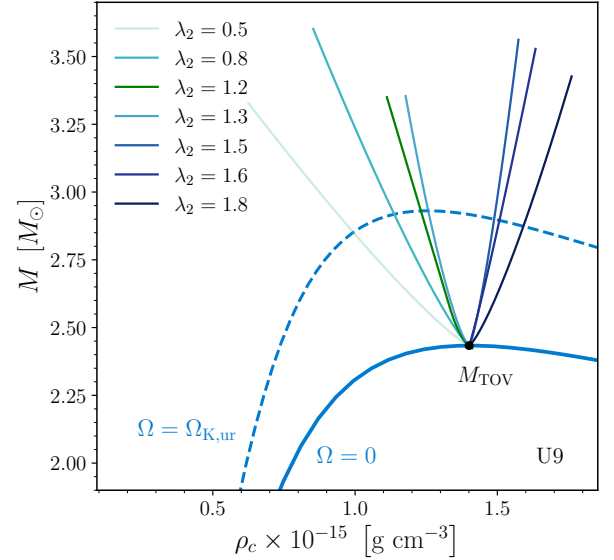


**Figure 14.** The same as in Fig. 5 for the U9 law but with different values of the parameters  $\lambda_2$  at fixed  $\lambda_1 = 2$ . Note how the increase in  $\lambda_2$  with constant  $\lambda_1$  leads to a change in the slope of the turning-point stability lines.

figure, the thick blue line shows the nonrotating solutions and the blue dashed line the Keplerian limit of uniform rotation. Besides the turning-point stability line of uniform rotation (dark blue line), we report the results of the  $j$ -constant law for  $\hat{A} = 3.33$  (violet line)<sup>3</sup> and for which the Keplerian limit of differential rotation is reached at a maximal mass of  $M_{\text{max}} = 3.41 M_\odot$  (violet star), as already reported by Weih et al. (2018). Unfortunately, this is also the only law of differential rotation for which a maximum mass on the Keplerian limit was found as extending the turning-point stability lines beyond the values reported in the figure (that are below the Keplerian limit) has turned out not to be possible from a computational point of view.

Other turning-point stability lines reported in Fig. 13 are for the U8 law with  $p = 1, q = 3, \lambda_1 = 1.5, \lambda_2 = 0.5$  (turquoise line; see also Fig. 2), the U9 law with  $p = 1, \lambda_1 = 2, \lambda_2 = 1.2$  (light-green line) and

<sup>3</sup> We note that this parameter choice represents the smallest value of  $\hat{A}$  for the “type-A” models in the classification of Ansorg et al. (2009).

$p = 1$ ,  $\lambda_1 = 3$ ,  $\lambda_2 = 2.8$  (light-blue line; see also Figs. 5 and 10), the U9+ law with  $p = 0.8$ ,  $\xi = 3$ ,  $\lambda_1 = 3$ ,  $\lambda_2 = 2.8$  (orange line; see also Fig. 10), and, finally, the CR law with  $\hat{f}_{\max}/\hat{f}_e = 0.82$ ,  $\beta = 0.95$ ,  $\gamma = 1.8$ ,  $A = 20$ ,  $\lambda_1 = 3$  (red line; see also Fig. 11). Beside the variety of behaviours and slopes in the turning-point stability lines shown in Fig. 13, what we find particularly remarkable is that all the differential rotation laws that best match the angular-velocity profiles deduced from BNS merger simulations (U9, U9+ and CR) actually have turning-point stability lines with positive slopes. To the best of our knowledge, this is the first time this universal behaviour has been reported, and highlights how merger remnants tend to have critical masses that increase with increasing central rest-mass density.

In order to establish what produces the change of slope in the turning-point stability lines, we explore stellar models described by the U9 differential-rotation law – which shows turning-point stability lines with both positive and negative slopes (see Figs. 5 and 10) – at fixed parameters  $p = 1$ ,  $\lambda_1 = 2$  and when varying the parameter  $\lambda_2$ , which changes the value of the equatorial angular velocity  $\Omega_e$  and therefore the angular-velocity profile.

In Fig. 14 we present the stability lines for the U9 law for seven different values  $\lambda_2 = 0.5, 0.8, 1.2, 1.3, 1.5, 1.6, 1.8$ . Note how the variation of the value of  $\lambda_2$  clearly provides a change in the slope, so that for sequences with  $0.5 \leq \lambda_2 \leq 1.3$  the slope of the turning-point stability line is negative, while for sequences with  $1.3 \leq \lambda_2 \leq 1.8$  the slope is positive. Recalling that  $\lambda_2 := \Omega_e/\Omega_c$  [Eq. (20)] and since  $\lambda_1 := \Omega_{\max}/\Omega_c$  [Eq. (19)] is kept fixed in Fig. 14, we can convert the threshold value in  $\lambda_2$  for the change of slope to a threshold value in the ratio  $\Omega_e/\Omega_{\max}$ . In other words, we conjecture that stellar models for which the equatorial angular velocity is about  $3/4$  times larger than the maximum, i.e.,  $\Omega_e \gtrsim 3/4 \Omega_{\max}$  will have turning-point stability lines with positive slopes. In addition, if the impact of the  $\lambda_1$  parameter is weak, it may also be possible to convert the threshold value in  $\lambda_2$  for the change of slope to a threshold value in the ratio  $\Omega_e/\Omega_c$ , thus concluding that stellar models in which the equatorial angular velocity is about 1.4 times larger than the value at the stellar center, i.e.,  $\Omega_e \gtrsim 1.4 \Omega_c$ , will have turning-point stability lines with positive slopes. While these results have been obtained for the U9 law and the DD2 EOS, it is possible that the general criteria deduced here for the appearance of turning-point stability lines with positive slopes, i.e.,  $\Omega_e \gtrsim 3/4 \Omega_{\max}$  and  $\Omega_e \gtrsim 1.4 \Omega_c$ , may be satisfied also by other differential-rotation laws and EOSs. We plan to investigate this conjecture in a forthcoming work.

Finally, in order to gain a better understanding of what are the actual differences in the stellar properties induced by the various rotation laws, we study in more detail the interior structure of three differentially rotating models having the same gravitational mass of  $M = 2.62 M_\odot$ <sup>4</sup> and relative to the uniform, the U8, the U9 and the CR rotation laws, respectively; these models are marked by circles in Fig. 13. The three panels in Fig. 15, which show, respectively, the radial profiles of the angular velocity, of the specific angular momentum and of the rest-mass density, clearly indicate that when keeping the gravitational mass constant, the three different rotation laws will produce three significantly different internal structures. In particular, taking the uniform-rotation law as the reference, it is clear from the left panel that the U8 law – for which the turning-point stability line has negative slope – leads to angular velocities that are almost always larger than for the uniformly rotating model, and

where the central angular velocity is considerably larger than that at the equator for this particular choice of parameters. By contrast, the CR law, – for which the turning-point stability line has a positive slope – has angular velocities that are systematically smaller than the uniform-rotation model. In this latter case, furthermore, the uniform-velocity core is much more extended and almost a factor four larger than in the U8-law models. The data relative to the additional U9 law can be considered as an intermediate case between the U8 and CR laws and hence the corresponding stellar model exhibits a behaviour that is in-between what discussed for the other two laws.

Finally, note that with the exception of the CR-law model, which is the most compact of the four stellar models, the other three models have rather similar radii, with the uniform-rotation model being the most extended and being followed by the U8 and U9-law models. At the same time, the density profiles are rather different. In particular, the U8-law model has the core with the lowest rest-mass density of the four models, while, by contrast, the CR-law model has the larger rest-mass densities in the inner regions of the star. This is not surprising and indeed what to be expected given that the angular velocity in the core of the CR-law model is the smallest and hence it provides the smallest centrifugal support. On the other hand, the angular velocity in the core of the U8-law model is the largest and hence it provides the strongest centrifugal support. A similar behaviour is found when comparing for models with the U9 law and having the same gravitational mass but different values of the  $\lambda_2$  parameter, i.e., equal-mass models in Fig. 14.

In summary, the panels in Fig. 15 clarify that differentially rotating stars with realistic differential-rotation laws near the turning-point stability line tend to have extended, slowly but uniformly rotating cores that have comparatively larger rest-mass densities. The fact that the U8-law does not reproduce well such a behaviour represents a very strong motivation towards the use of more realistic laws such as U9+ or CR.

## 6 CONCLUSIONS

Modelling the properties of the remnants of core-collapse supernovae or of BNS mergers has a long history and has reached a high degree of sophistication, with a series of various differential-rotation laws that have been proposed over the years. The most recent of such laws – normally referred to as Uryu laws of differential rotation – have been inspired by simulations and have among the most important features: (i) a slowly and uniformly rotating core; (ii) a rapid increase in the angular velocity in the outer regions of the merger remnant; (iii) a radial fall-off reflecting a Keplerian profile. While these laws have been used extensively in the literature and studied to explore the space of solutions of differentially rotating stars, they do not always represent a good match to the simulations. To further improve the level of realism in the construction of equilibrium models of differentially rotating neutron stars, we have here reconsidered this problem starting from the actual data.

In particular, we have analysed the results of three, state-of-the-art BNS merger simulations performed with different and realistic EOSs and mass ratios, and have extracted from them the quasi-stationary rotational properties of the remnants, both in terms of azimuthally- and time-averaged profiles of the angular velocity and of the specific angular momentum. This analysis has been useful to study the existence of universal features in the angular-velocity profile and to point out a simple criterion to recognise the transition between the “core” of the remnant and the “disc”, that is, the portion of the HMNS whose angular-velocity profile follows a Keplerian behaviour.

<sup>4</sup> Note that this mass is smaller than the initial gravitational mass of the DD2 binary (cf. Table 1) because it does not include the mass radiated in gravitational waves or the mass in the remnant disc.



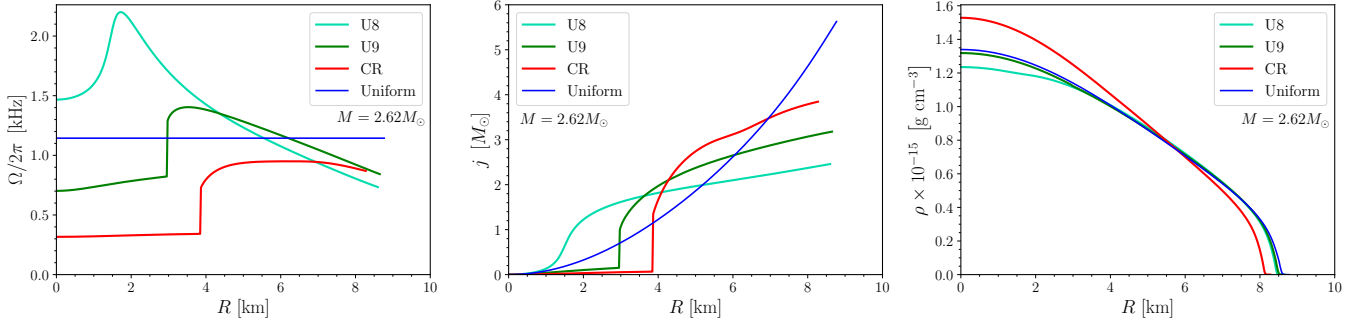


**Figure 15.** Rotational and structural properties of the four stellar models with mass  $M = 2.62 M_\odot$  and marked as filled circles on the stability lines in Fig. 13. Shown are the U8 law (light blue;  $p = 1, q = 3, \lambda_1 = 1.5, \lambda_2 = 0.5$ ) in turquoise, the U9 law (green;  $p = 1, \lambda_1 = 2, \lambda_2 = 1.2$ ) the CR law (red). From left to right we report the radial profiles of the angular velocity (left panel), of the specific angular momentum (middle panel) and of the rest-mass density (right panel).

More specifically, it was possible to realise that in the remnant core the angular velocity exhibits a robust and generic linear behaviour in terms of the logarithm of the rest-mass density. Furthermore, the departure from this linear behaviour also corresponds to the location in the remnant where the Keplerian flow starts, so that it is simple to mark the beginning of the remnant disc as the location where the angular velocity is no longer linearly proportional to the logarithm of the rest-mass density. Interestingly, this position does not correspond to the maximum of the angular velocity, but is located at larger radii.

In addition to the analysis of the data from numerical simulations, we have extensively tested and modified the *Hydro-RNS* code, whose public version is unfortunately unable to reproduce the rather extreme differential-rotation profiles that are present in realistic simulations, in particular for equatorial angular velocities that are comparable or larger than the central ones, i.e., with  $\Omega_e \gtrsim \Omega_c$ . In this way, after reviewing the basic properties of the traditional U8 and U9 Uryu laws, we have provided evidence of the code’s ability to reproduce published results and to extend the ranges in which they have been studied so far.

The use of the differential-rotation profiles extracted from the simulations has allowed us to realise that while the U9 law can provide a reasonable approximation of the data, the fidelity can be further improved after a simple extension of the law in terms of an additional exponent, leading to what we have referred to as the U9+ law. However, both the U9 and the U9+ laws provide a rather inaccurate description in the outer layers of the remnants, where the angular velocity and the rest-mass density are low. To counter that, we have devised a novel law of differential rotation, that we refer to as the CR law, which, thanks to the addition of new parameters, allows to reproduce the angular-velocity profiles also well beyond the nominal stellar surface and with relative differences that are always below 5%.

A particularly interesting and important aspect of the research carried out here is that related to the determination of the dynamical stability line obtained from the turning-point criterion, namely, by the stability line marking the maximum (turning point) of the gravitational mass along sequences of constant angular momentum. Although this line reflects only a sufficient condition for the dynamical collapse to rotating black holes, its global properties are still largely unknown. Thanks to the large number of differentially rotating models computed here, it has been possible to carry out the first systematic study of the properties of turning-point stability lines in realistic (and non-realistic) laws of differential rotation. A particularly surprising result obtained in this way is that the slope of the stability line, namely, the sign of the derivative  $\partial M / \partial \rho_c|_{\text{tp}}$  depends

on the properties of the law of differential rotation and is not necessarily negative, as customary for the  $j$ -constant or the U8 laws. In particular, we have shown that the U9+ and CR laws (but also the U9 law with a suitable choice of parameters) – which provide an accurate representation of the properties of the post-merger remnant – actually lead to turning-point stability lines where the maximum mass grows with the central rest-mass density, i.e., with  $\partial M / \partial \rho_c|_{\text{tp}} > 0$ . We believe this reflects closely the properties of the BNS-merger remnant, which has a larger amount of angular momentum in the outer layers and a slowly rotating core, so that the reduced centrifugal support leads also to larger central rest-mass densities. On the basis of the EOSs and differential rotation laws studied here, we conjecture that stellar models for which the equatorial angular velocity is about 3/4 times larger than the maximum, i.e.,  $\Omega_e \gtrsim 3/4 \Omega_{\text{max}}$  will exhibit turning-point stability lines with  $\partial M / \partial \rho_c|_{\text{tp}} > 0$ .

The systematic and comprehensive analysis presented here can be extended and improved in a number of ways. First, by exploring the post-merger properties of remnants produced with other EOSs so as to validate the robustness of the proposed U9+ and CR laws. Particularly important in this respect will be exploration of a broader range of mass ratios as they seem to exhibit somewhat different differential-rotation laws. Second, by improving the convergence properties of *Hydro-RNS* and hence compute the Keplerian line of differentially rotating models that so far in the literature has been computed only for the simpler  $j$ -constant differential-rotation law. Third, compute the location of the neutral-stability line (Takami et al. 2011) and determine its location with respect to the turning-point stability line. Finally, use numerical simulations of dynamical spacetimes to explore the equilibrium properties of the turning-point and neutral stability lines to determine necessary and sufficient conditions for collapse to rotating black holes, thus confirming also for more realistic differentially rotating stars the analysis carried out for the  $j$ -constant law (Weih et al. 2018; Szewczyk et al. 2023). We plan to explore some of these topics in future works.

## ACKNOWLEDGEMENTS

We thank K. Topolski, M. Chabanov and C. Ecker for providing the data of the numerical simulations. We are also grateful to P. Iosif, C. Krüger and N. Stergioulas for help with the code and useful comments. This research is supported by the European Research Council Advanced Grant “JETSET: Launching, propagation and emission of relativistic jets from binary mergers and across mass scales” (grant no. 884631). LR acknowledges the Walter Greiner Gesellschaft zur Förderung der physikalischen Grundlagenforschung e.V. through the

Carl W. Fueck Laureatus Chair. The calculations were performed on the local ITP Supercomputing Clusters Iboga and Calea and on HPE Apollo HAWK at the High Performance Computing Center Stuttgart (HLRS) under the grant BNSMIC.

## DATA AVAILABILITY

Data available on request. The data underlying this article will be shared on reasonable request to the corresponding author.

## APPENDIX A: ON THE U8 MODELS AND THE DD2 SIMULATION

To facilitate the reproducibility of our results, in this Appendix we provide additional information on the computed stellar models with the U8 and on the evolution of the remnant properties of the BNS simulation with a DD2 EOS. More specifically, we present in Table A1 the most important properties of the equilibrium stellar models computed with Hydro-RNS and the U8 rotational law when keeping the central rest-mass density at  $\rho_c = 8.024 \times 10^{14} \text{ g cm}^{-3}$  and the axis ratio at  $R_p/R_e = 0.8$  (see Figs. 1 and 3 in the main text).

Similarly, we present in Fig. A1 a more refined in time evolution of various quantities extracted from the BNS merger simulation performed with the DD2 EOS. In particular, from the top right and in a clock-wise sense we report the evolution of the radial profiles of various quantities as the rest-mass density  $\rho$ , the temperature  $T$ , the specific angular momentum  $j$  and the angular velocity  $\Omega$ . All quantities are evaluated on the equatorial plane ( $z = 0$ ) averaged in the azimuthal direction and in time in an interval of 0.1 ms and spanning a window in time  $5 \text{ ms} < t - t_{\text{mer}} < 23 \text{ ms}$  (solid lines from red to blue; some of this data was also shown in Fig. 7, although with a lower cadence).

Note how the remnant is extremely dynamical up to  $t - t_{\text{mer}} \simeq 10 \text{ ms}$ , but also that soon after it reaches a quasi-stationary equilibrium lasting from  $t - t_{\text{mer}} \simeq 12 \text{ ms}$  till the end of the simulation and in which all quantities settle to their typical behaviour: a high-density, low angular velocity and cold core surrounded by a low-density, high angular velocity and hot mantle. Interestingly, due to the differential rotation and a higher rotation frequency off from the center, the star heats up into a ring around the center, reaching temperatures up to 35 MeV.<sup>5</sup>

## APPENDIX B: COMPUTING EQUILIBRIA WITH THE CR LAW

This Appendix is dedicated to the numerical strategy we have implemented in order to obtain numerical solutions with the new and more complex CR differential rotation law. We recall that it has free parameters  $\beta$ ,  $\gamma$ ,  $A$ ,  $\lambda_1$ , and  $j_{\text{max}}/j_e$  which, together, control the shape of the profile. In particular, the parameter  $\lambda_1$  regulates the maximum angular velocity and can be read off from the ratios of the angular velocities from the merger-profiles. The parameter  $\beta$  controls instead the slope of the angular velocity for angular momenta smaller than  $j_{\text{max}}$ , which tends to become constant (linear behaviour) for smaller values of  $\beta$ . The parameters  $A$  and  $\gamma$  are responsible for the part with

angular momenta larger than  $j_{\text{max}}$ , with  $\gamma$  controlling how far from the maximum the decreasing part is extended, and  $A$  regulating the slope of the angular velocity in the Keplerian region. Note that larger values of the ratio  $\gamma/A$  yield profiles that extend to larger angular momenta.

Once a set of parameters of the CR law has been chosen, we can compute  $\lambda_2$  from the definition (53) at  $j = j_e$  and when  $j \geq j_{\text{max}}$  part

$$\lambda_2 = \lambda_1 - \lambda_1 A \left( \frac{j_e}{j_{\text{max}}} - 1 \right)^{2\gamma}. \quad (\text{B1})$$

This fixes the value of  $\lambda_2$ , which can be employed in the Euler equation (5) to find  $\Omega_e$  and hence  $\Omega_c = \Omega_e/\lambda_2$ .

While the CR law provides a more accurate representation of the remnant rotational properties, it also offers additional challenges during the numerical calculation and can easily lead to a loss of convergence in the iterative procedure employed by Hydro-RNS in computing a solution. In particular, for large values of  $\lambda_1 = \Omega_{\text{max}}/\Omega_c$ , the range of possible guesses for  $r_e$  and of the corresponding solutions of  $\Omega_e$  grows substantially. In addition, if the guess for  $r_e$  is rather different from the one for which a solution exists, the code fails to converge because no solution with the guessed  $\Omega_e$  can be found with the Euler equation. It is in principle possible to manually control the iterations of  $r_e$  and to extend the range of search of  $\Omega_e$  so that a solution is found, but this is tedious and not robust.

However, an approach that tackles these problems consists “blending” the solution with the new CR rotation law with the solution obtained with the U9 law, which is less accurate but less challenging in the regions of large specific angular momentum. Hence, we introduce a smooth transition from the converging U9 rotation law to the new CR law via a simple linear combination

$$\Omega(j) = \alpha \Omega_{\text{U9+}}(j) + \beta \Omega_{\text{CR}}(j), \quad (\text{B2})$$

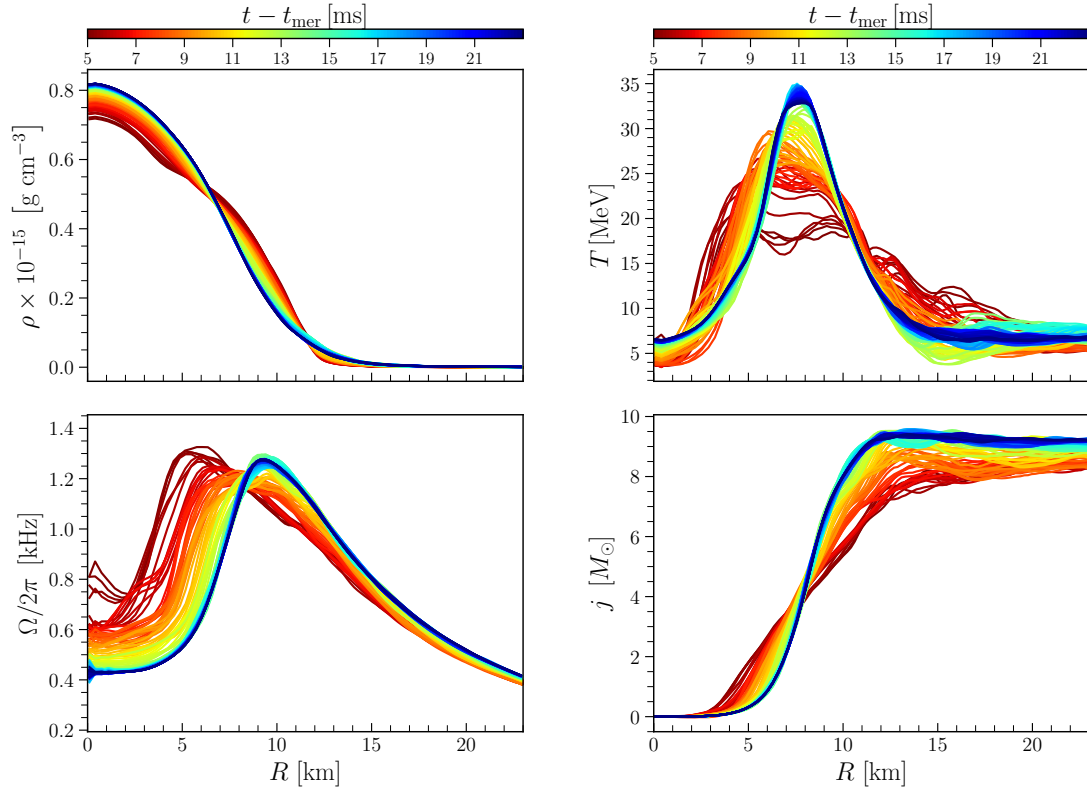
where  $\alpha, \beta \in [0, 1]$  and  $\alpha + \beta = 1$ . Hence, starting with  $\alpha = 1, \beta = 0$  and progressively marching to a situation in which  $\alpha = 0, \beta = 1$ , the Hydro-RNS code can find equilibrium solutions with axis ratios that are larger than those allowed by the U9+ rotation law. Clearly, the strategy adopted in the blending (B2) with the U9 law can be employed also with other differential-rotation laws.

Figure B1 illustrates the result of this approach by showing how an equilibrium solution with the CR law with  $j_{\text{max}}/j_e = 0.82, \beta = 0.95, \gamma = 1.8, A = 20, \lambda_1 = 3$  (red thick line) can be obtained from an initial U9+ law with  $p = 1, \xi = 1, \lambda_1 = 2, \lambda_2 = 1.6$  (blue thick line) via a sequence of intermediate solutions which represent the various flavours of the blending (B2) (blue and red thin lines). The final solution is compared with the angular velocity profile of the DD2 BNS simulation (black thick line) at  $t - t_{\text{mer}} = 20 \text{ ms}$ , showing the superior accuracy of the new CR law.

## REFERENCES

- Abdikamalov E. B., Ahmedov B. J., Miller J. C., 2009, *Mon. Not. R. Astron. Soc.*, **395**, 443
- Abdikamalov E. B., Ott C. D., Rezzolla L., Dessart L., Dimmmeier H., Marek A., Janka H.-T., 2010, *Phys. Rev. D*, **81**, 044012
- Ansorg M., Gondek-Rosińska D., Villain L., 2009, *Mon. Not. R. Astron. Soc.*, **396**, 2359
- Baiotti L., Rezzolla L., 2017, *Rept. Prog. Phys.*, **80**, 096901
- Baiotti L., De Pietri R., Manca G. M., Rezzolla L., 2007, *Phys. Rev. D*, **75**, 044023
- Baiotti L., Giacomazzo B., Rezzolla L., 2008, *Phys. Rev. D*, **78**, 084033

<sup>5</sup> Although the remnants have high temperatures in the fast-rotating regions, for simplicity, we use cold  $\beta$ -equilibrium slices of the EOSs to construct models with Hydro-RNS.



**Figure A1.** The same as in Fig. 7 but for a higher cadence of 0.1 ms. The data refers to the BNS merger simulation with the DD2 EOS and shows, in addition, the radial profiles of the rest-mass density (top-left panel) and temperature (top-right panel).

**Table A1.** Physical quantities for stellar models computed with the U8 rotation law, the DD2 EOS, a fixed central rest-mass density of  $\rho_c = 8.024 \times 10^{14} \text{ g cm}^{-3}$  and fixed axis ratio  $R_p/R_e = 0.8$ .

Model	$\hat{A}$	$\hat{B}$	$p$	$q$	$M_0$ [ $M_\odot$ ]	$M$ [ $M_\odot$ ]	$J$ [ $M_\odot^2$ ]	$T/ W $ $\times 10^{-2}$	$\Omega_c/2\pi$ [kHz]	$\Omega_{\max}/2\pi$ [kHz]	$\Omega_e/2\pi$ [kHz]	$\Omega_K/2\pi$ [kHz]	$R_e$ [km]	$r_e$ [km]
A	0.808	0.467	1.00	3.00	2.653	2.287	2.074	5.198	0.915	2.290	0.458	1.711	9.268	6.731
B	0.930	0.865	1.00	3.00	2.666	2.302	2.385	6.444	1.067	1.600	0.533	1.677	9.419	6.853
C	1.427	0.988	1.00	3.00	2.667	2.310	2.676	7.215	0.640	1.279	0.639	1.627	9.637	7.049
D	2.042	1.414	1.00	3.00	2.630	2.283	2.639	7.200	0.535	1.071	0.803	1.564	9.879	7.318
X	0.854	0.591	1.00	3.00	2.659	2.295	2.214	5.663	0.977	1.955	0.489	1.697	9.332	6.781
E	1.8	1.2	1.00	3.00	2.650	2.299	2.707	7.399	0.543	1.135	0.729	1.590	9.785	7.206
F	1.8	1.6	1.00	3.00	2.641	2.291	2.680	7.183	0.674	1.050	0.774	1.578	9.818	7.249
G	1.3	1.0	1.00	3.00	2.669	2.310	2.641	7.070	0.734	1.310	0.621	1.636	9.596	7.009
H	2.3	1.8	1.00	3.00	2.603	2.260	2.488	6.626	0.586	1.028	0.904	1.538	9.955	7.429
I	1.8	1.4	1.25	3.00	2.639	2.290	2.676	7.272	0.606	1.095	0.768	1.574	9.840	7.271
J	1.8	1.4	1.50	3.00	2.635	2.287	2.655	7.292	0.595	1.114	0.777	1.569	9.861	7.294
K	1.8	1.4	1.00	5.00	2.647	2.297	2.704	7.379	0.587	1.134	0.723	1.585	9.805	7.227
L	1.8	1.4	1.00	7.00	2.658	2.306	2.740	7.511	0.574	1.172	0.707	1.587	9.807	7.221
Y	1.8	1.4	1.00	3.00	2.645	2.294	2.698	7.279	0.614	1.083	0.756	1.582	9.810	7.237

Baumgarte T. W., Shapiro S. L., Shibata M., 2000, *Astrophys. J. Lett.*, **528**, L29

Bozzola S., Gourgoulhon E., Salgado M., Marck J. A., 1993, *Astron. and Astrophys.*, **278**, 421

Bozzola G., 2021, *The Journal of Open Source Software*, **6**, 3099

Bozzola G., Stergioulas N., Bauswein A., 2018, *Mon. Not. R. Astron. Soc.*, **474**, 3557

Bozzola G., Espino P. L., Lewin C. D., Paschalidis V., 2019, *European Physical Journal A*, **55**, 149

Breu C., Rezzolla L., 2016, *Mon. Not. R. Astron. Soc.*, **459**, 646

Burrows A., Dessart L., Livne E., Ott C. D., Murphy J., 2007, *Astrophys. J.*, **664**, 416

Camelio G., Dietrich T., Rosswog S., Haskell B., 2021, *Phys. Rev. D*, **103**, 063014

Chabanov M., Tootle S. D., Most E. R., Rezzolla L., 2023, *Astrophys. J. Lett.*, **945**, L14

Chi-Kit Cheong P., Muhammed N., Chawhan P., Duez M. D., Foucart F., 2024, *arXiv e-prints*, p. arXiv:2402.18529

Cioffi R., Kastaun W., Giacomazzo B., Endrizzi A., Siegel D. M., Perna R., 2017, *Phys. Rev. D*, **95**, 063016

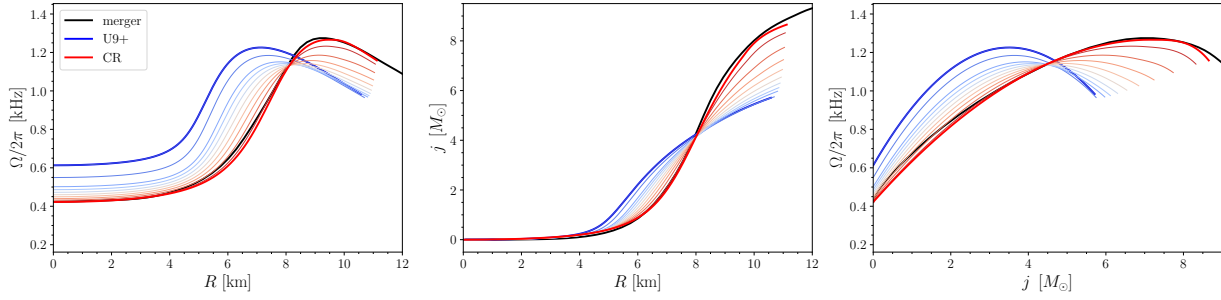


**Figure B1.** “Blending” of the rotational properties of stellar models with the U9+ and CR differential-rotation laws to transit from a pure-U9+ model (thick blue line) to a pure-CR model (thick red line) that provides an accurate description of the DD2 merger remnant (thick black line). All models obey the DD2 EOS, have a central rest-mass density of  $\rho_c = 8.024 \times 10^{14} \text{ g cm}^{-3}$  and an axis ratio  $R_p/R_e = 0.7$ .

- Cook G. B., Shapiro S. L., Teukolsky S. A., 1992, *Astrophys. J.*, **398**, 203
- De Pietri R., Feo A., Font J. A., Löffler F., Maione F., Pasquali M., Stergioulas N., 2018, *Phys. Rev. Lett.*, **120**, 221101
- Demircik T., Ecker C., Järvinen M., 2020, arXiv e-prints, p. arXiv:2009.10731
- Demircik T., Ecker C., Järvinen M., 2022, *Phys. Rev. X*, **12**, 041012
- Dessart L., Burrows A., Ott C. D., Livne E., Yoon S. C., Langer N., 2006, *ApJ*, **644**, 1063
- Dimmelmeier H., Stergioulas N., Font J. A., 2006, *Mon. Not. R. Astron. Soc.*, **368**, 1609
- Duez M. D., Liu Y. T., Shapiro S. L., Shibata M., Stephens B. C., 2006, *Phys. Rev. D*, **73**, 104015
- East W. E., Paschalidis V., Pretorius F., Tsokaros A., 2019, *Phys. Rev. D*, **100**, 124042
- Ecker C., Järvinen M., Nijs G., van der Schee W., 2020, *Phys. Rev. D*, **101**, 103006
- Espino P. L., Paschalidis V., 2019, *Phys. Rev. D*, **99**, 083017
- Espino P. L., Paschalidis V., Baumgarte T. W., Shapiro S. L., 2019, *Phys. Rev. D*, **100**, 043014
- Font J. A., et al., 2002, *Phys. Rev. D*, **65**, 084024
- Franceschetti K., Del Zanna L., 2020, *Universe*, **6**, 83
- Franci L., De Pietri R., Dionysopoulou K., Rezzolla L., 2013, *Journal of Physics Conference Series*, **470**, 012008
- Friedman J. L., Ipser J. R., Sorkin R. D., 1988, *Astrophys. J.*, **325**, 722
- Giacomazzo B., Rezzolla L., Stergioulas N., 2011, *Phys. Rev. D*, **84**, 024022
- Gondek-Rosińska D., Kowalska I., Villain L., Ansorg M., Kucaba M., 2017, *Astrophys. J.*, **837**, 58
- Goussard J., Haensel P., Zdunik J. L., 1998, *Astron. and Astrophys.*, **330**, 1005
- Haas R., et al. 2020, The Einstein Toolkit, doi:10.5281/zenodo.4298887, https://doi.org/10.5281/zenodo.4298887
- Hanauske M., Takami K., Bovard L., Rezzolla L., Font J. A., Galeazzi F., Stöcker H., 2017, *Phys. Rev. D*, **96**, 043004
- Hanauske M., Weih L. R., Stöcker H., Rezzolla L., 2021, *Eur. Phys. J. ST*, **230**, 543
- Hempel M., Schaffner-Bielich J., 2010a, *Nuclear Physics A*, **837**, 210
- Hempel M., Schaffner-Bielich J., 2010b, *Nucl. Phys.*, **A837**, 210
- Iosif P., Stergioulas N., 2021, *Mon. Not. Roy. Astron. Soc.*, **503**, 850
- Iosif P., Stergioulas N., 2022, *Mon. Not. Roy. Astron. Soc.*, **510**, 2948
- Ishii T., Järvinen M., Nijs G., 2019, *JHEP*, **07**, 003
- Järvinen M., Kiritsis E., 2012, *JHEP*, **03**, 002
- Kastaun W., Galeazzi F., 2015, *Phys. Rev. D*, **91**, 064027
- Komatsu H., Eriguchi Y., Hachisu I., 1989a, *Mon. Not. R. Astron. Soc.*, **237**, 355
- Komatsu H., Eriguchi Y., Hachisu I., 1989b, *Mon. Not. R. Astron. Soc.*, **239**, 153
- Krüger C., Gaertig E., Kokkotas K. D., 2010, *Phys. Rev. D*, **81**, 084019
- Lasota J.-P., Haensel P., Abramowicz M. A., 1996, *Astrophys. J.*, **456**, 300
- Lin L. M., Cheng K. S., Chu M. C., Suen W. M., 2006, *Astrophys. J.*, **639**, 382
- Loeffler F., et al., 2012, *Class. Quantum Grav.*, **29**, 115001
- Lyford N. D., Baumgarte T. W., Shapiro S. L., 2003, *Astrophys. J.*, **583**, 410
- Manca G. M., Baiotti L., DePietri R., Rezzolla L., 2007, *Class. Quantum Grav.*, **24**, S171
- Muhammed N., et al., 2024, arXiv e-prints, p. arXiv:2403.05642
- Müller B., 2024, arXiv e-prints, p. arXiv:2403.18952
- Musolino C., Ecker C., Rezzolla L., 2024, *Astrophys. J.*, **962**, 61
- Ng H. H.-Y., Jiang J.-L., Musolino C., Ecker C., Tootle S. D., Rezzolla L., 2024, *Phys. Rev. D*, **109**, 064061
- Ott C. D., Burrows A., Thompson T. A., Livne E., Walder R., 2006, *Astrophys. J. Suppl. Ser.*, **164**, 130
- Paschalidis V., 2017, *Classical and Quantum Gravity*, **34**, 084002
- Passamonti A., Andersson N., 2020, *Monthly Notices of the Royal Astronomical Society*, **498**, 5904
- Rezzolla L., Zanotti O., 2013, *Relativistic Hydrodynamics*. Oxford University Press, Oxford, UK, doi:10.1093/acprof:oso/9780198528906.001.0001
- Rezzolla L., Lamb F. K., Shapiro S. L., 2000, *Astrophys. J. Lett.*, **531**, L139
- Rezzolla L., Baiotti L., Giacomazzo B., Link D., Font J. A., 2010, *Class. Quantum Grav.*, **27**, 114105
- Sá P. M., 2004, *Phys. Rev. D*, **69**, 084001
- Saijo M., Baumgarte T. W., Shapiro S. L., 2003, *Astrophys. J.*, **595**, 352
- Shibata M., Karino S., Eriguchi Y., 2002, *Mon. Not. R. Astron. Soc.*, **334**, L27
- Shibata M., Taniguchi K., Uryū K., 2003, *Phys. Rev. D*, **68**, 084020
- Staykov K. V., Doneva D. D., Heisenberg L., Stergioulas N., Yazadjiev S. S., 2023, *Phys. Rev. D*, **108**, 024058
- Stergioulas N., 1998, *Living Rev. Relativ.*, **1**, 8
- Stergioulas N., Friedman J. L., 1995, *Astrophys. J.*, **444**, 306
- Stergioulas N., Apostolatos T. A., Font J. A., 2004, *Mon. Not. R. Astron. Soc.*, **352**, 1089
- Studzińska A. M., Kucaba M., Gondek-Rosińska D., Villain L., Ansorg M., 2016, *Mon. Not. R. Astron. Soc.*, **463**, 2667
- Szewczyk P., Gondek-Rosińska D., Cerdá-Durán P., 2023, *Acta Phys. Polon. Suppl.*, **16**, 8
- Szkudlarek M., Gondek-Rosińska D., Villain L., Ansorg M., 2019, *Astrophys. J.*, **879**, 44
- Takami K., Rezzolla L., Yoshida S., 2011, *Mon. Not. R. Astron. Soc.*, **416**, L1
- Takami K., Rezzolla L., Baiotti L., 2014, *Phys. Rev. Lett.*, **113**, 091104
- Takami K., Rezzolla L., Baiotti L., 2015, *Phys. Rev. D*, **91**, 064001
- Tassoul J.-L., 1978, *Theory of Rotating Stars*. Princeton University Press
- Togashi H., Nakazato K., Takehara Y., Yamamuro S., Suzuki H., Takano M., 2017, *Nucl. Phys.*, **A961**, 78
- Tsokaros A., Ruiz M., Shapiro S. L., 2020, *Phys. Rev. D*, **101**, 064069
- Typel S., Röpke G., Klahn T., Blaschke D., Wolter H. H., 2010, *Phys. Rev. C*, **81**, 015803
- Uryū K., Tsokaros A., Baiotti L., Galeazzi F., Taniguchi K., Yoshida S., 2017, *Phys. Rev. D*, **96**, 103011
- Weih L. R., Most E. R., Rezzolla L., 2018, *Mon. Not. R. Astron. Soc.*, **473**, L126
- Weih L. R., Hanauske M., Rezzolla L., 2020, *Phys. Rev. Lett.*, **124**, 171103
- Xie X., Hawke I., Passamonti A., Andersson N., 2020, *Phys. Rev. D*, **102**, 044040



- Zhou E., Tsokaros A., Uryu K., Xu R., Shibata M., 2019, [Phys. Rev. D](#), 100, 043015
- Zink B., Korobkin O., Schnetter E., Stergioulas N., 2010, *Phys. Rev. D*, 81, 084055

This paper has been typeset from a  $\text{\LaTeX}$  file prepared by the author.